Sigrid Benedikte Otterlei Sunde

Energy Yield Analysis and Evaluation of Software Used for Different Configurations of Bifacial Photovoltaic Modules in Trondheim, Norway

Master's thesis in Materials Science and Chemical Engineering
Supervisor: Marisa Di Sabatino
Co-supervisor: Martin Bellmann (SINTEF), Alessandro Nocente (SINTEF) and Gabriele Lobaccaro (NTNU)
June 2022

Master's thesis

NTNU
Norwegian University of
Science and Technology

SINTEF

Sigrid Benedikte Otterlei Sunde

Energy Yield Analysis and Evaluation of Software Used for Different Configurations of Bifacial Photovoltaic Modules in Trondheim, Norway

NTNU
Norwegian University of
Science and Technology

Preface

This master's thesis marks the end of my degree at the Norwegian University of Science and Technology (NTNU). The paper was written for the Department of Materials Science and Engineering in cooperation with SINTEF Industry. The work was carried out during the Spring of 2022 on campus Gløshaugen at NTNU in Trondheim, Norway.

I would like to thank my supervisor Marisa Di Sabatino(NTNU), and co-supervisors Gabriele Lobaccaro(NTNU), Alessandro Nocente(SINTEF), and Martin Bellmann(SINTEF) for their help, guidance, and time throughout the semester. An additional thanks to Martin Bellmann, who has provided me with the measured data needed, and close follow-up. Lastly, I would like to thank my friends for making my time in Trondheim the best.

Sigrid Benedikte Otterlei Sunde
Trondheim, June 2022

Abstract

The total market share of bifacial photovoltaics (PV) panels is increasing as the prices of the modules are competitive with monofacial PV panels. Bifacial PV can receive irradiance from both the front and the rear sides, which results in higher energy yield and energy density than monofacial panels. However, there is little research on bifacial PV in the Nordic climate, which is characterised by long, mild days in the summer, and short, cold days in the winter. The literature on the best configuration for bifacial PV panels at high latitudes is ambiguous, and research on optimal sky models used for the modelling of PV systems in the Nordics is lacking.

In this master's thesis, four different configurations of bifacial panels, located at campus Gløshaugen at NTNU in Trondheim, are investigated. This is an outdoor laboratory installed on the rooftop of Sentralbygg 1, called "Alfa Centauri", and is owned and operated by SINTEF. The first configuration has a 44°tilt towards the South, then there is one vertical panel facing East/West and another vertical facing South/North. The last is a two-axis tracking system that follows the Sun throughout the day. The measured values from this system are compared with simulated energy production from PV*SOL and PVsyst. In addition, an analysis of the different decomposition models, the modelling diffuse horizontal irradiance (DHI), the transposition models, and the modelling irradiance in the plane of the module, available in PV*SOL and PVsyst, is conducted.

Based on the simulation results, the 44°tilt towards the South shows the highest energy production of the fixed configurations. Of the vertical configurations, the South/North produces more energy annually than the East/West configuration. However, the difference in production is small and both configurations can be advantageous depending on the consumer. For example, in a household, energy consumption is high in the morning and the late afternoon; therefore, an East/West configuration would be beneficial since it produces more energy in these time slots than the South/North configuration. The best combinations of decomposition and transposition models available in PV*SOL are Erbs + Perez and Orgill + Hay for the 44°tilt. Erbs + Perez also showed good results for the vertical South/North and the tracking configuration, while Reindl + Liu showed the best results for the East/West configuration. For PVsyst, Erbs + Perez was the best model for all configurations.

Sammendrag

Markedsandelen til tosidige solcellemoduler øker ettersom prisene på modulene konkurrerer med ensidige PV-moduler. Tosidige PV-moduler kan absorbere irradians fra både fram- og bakside, noe som resulterer i et høyere energiutbytte og energitetthet enn for ensidige paneler. Det er imidlertid lite forskning på temaet i det nordiske klimaet. Nordisk klima er preget av lange, milde dager om sommeren og korte, kalde dager om vinteren. Spesielt mangler det litteratur på beste konfigurasjon for tosidige PV-paneler, samt forskning på beste modeller å bruke for modellering av PV systemer for breddegrader langt nord.

I denne masteroppgaven undersøkes fire ulike konfigurasjoner av tosidige paneler plassert på campus Gløshaugen i Trondheim. Dette er et utendørs laboratorium installert på taket av Sentralbygg 1, kalt "Alfa Centauri" som eies og drives av SINTEF. Den første konfigurasjonen har en 44°tilt mot sør, deretter er det en vertikalt vendt mot øst/vest, og en annen vertikalt vendt mot sør/nord. Den siste er et to-akset trackingsystem, som følger solen gjennom dagen. Systemets målte verdier sammenlignes med simulert energiproduksjon fra PV*SOL og PVsyst. I tillegg utføres en analyse av de forskjellige dekomponeringsmodellene, som modellerer DHI, og transposisjonsmodeller, som modellerer irradians i modulens plan. Analysen er basert på tilgengelige modeller i PV*SOL og PVsyst.

Basert på simuleringsresultatene fra denne oppgaven, viser 44°tilt mot sør den høyeste energiproduksjonen av de fastmonterte konfigurasjonene. Av de vertikale konfigurasjonene produserer sør/nord mer energi årlig enn øst/vest-konfigurasjonen. Imidlertid er forskjellen i produksjon liten og begge konfigurasjoner kan være fordelaktige avhengig av forbruket. For eksempel vil energiforbruket i en husholdning normalt være høyt om morgenen og ettermiddagen. Her vil en øst/vest-konfigurasjon være fordelaktig, siden denne konfigurasjonen produserer mer i disse tidsrommene. De beste kombinasjonene av dekomponering- og transposisjonsmodellene tilgjengelig i PV*SOL, er Erbs + Perez og Orgill + Hay for 44°tilt. Erbs + Perez viste også gode resultater for den vertikale sør/nord- og trackingkonfigurasjonen, mens Reindl + Liu viste de beste resultatene for øst/vest-konfigurasjonen. I PV*syst er også Erbs + Perez den beste modellen for alle konfigurasjonene.

Nomenclature

α_s elevation angle

β tilt angle

η efficiency

γ azimuth angle

θ_z zenith angle

A area

E_g energy of the bandgap

G generation rate

I_0 dark saturation current

I_a reflected radiation

I_b direct radiation

I_d diffuse radiation

I_g global radiation

I_m maximum current

I_{SC} short circuit current

K kelvin

k Boltzmann's constant

L_e diffusion length of electrons

L_h diffusion length of holes

P_S power input from the sun

P_{MP} maximum power point

q charge

T temperature

V_m maximum voltage

V_{OC} open circuit voltage

Acronyms

AM air mass. 8, 12, 13

BG bifacial gain. 4, 5

DC direct current. 22

DHI diffuse horizontal irradiance. II, III, 12, 13

DNI direct normal irradiance. 12, 47

FF fill factor. 10

GHI global horizontal irradiance. 12

NICE New Industrial Cell Encapsulation. 20

NTNU the Norwegian University of Science and Technology. I, II, 2

PV photovoltaics. II, III, 1–3, 6–8, 20, 53

STC Standard test conditions. 8, 13

Contents

List of Figures

List of Tables

1 Introduction

1.1 Background and motivation

The global climate crisis threatens all living life on Earth. Climate change is affecting economies, weather patterns, and the climate is becoming more extreme. The Intergovernmental Panel on Climate Change (IPCC) released a report in 2021 revealing that the Earth is heating up faster than originally believed.[5] The report states that greenhouse gas emissions must be reduced to net zero by 2050 if we are to preserve a liveable climate. In addition, global energy demand is increasing. The European Commission recently issued a plan to rapidly reduce the dependence on Russian fossil fuels and accelerate the green transition. Solar energy is reported to be the fastest and cheapest renewable energy source to expand, to reduce the effect of the energy crisis that Europe is currently experiencing.[6] The energy and climate crisis are also affecting Norway and solar power installations are increasing rapidly. At the beginning of 2021, 160 MW of solar power was installed in Norway, whereas 40 MW was installed in 2020. A further exponential increase is expected; NVE predicts a production of 7 TWh within 2040, illustrated in Figure 1.1. Therefore, this fast-growing field is important to gain knowledge about and conduct research on.[1]
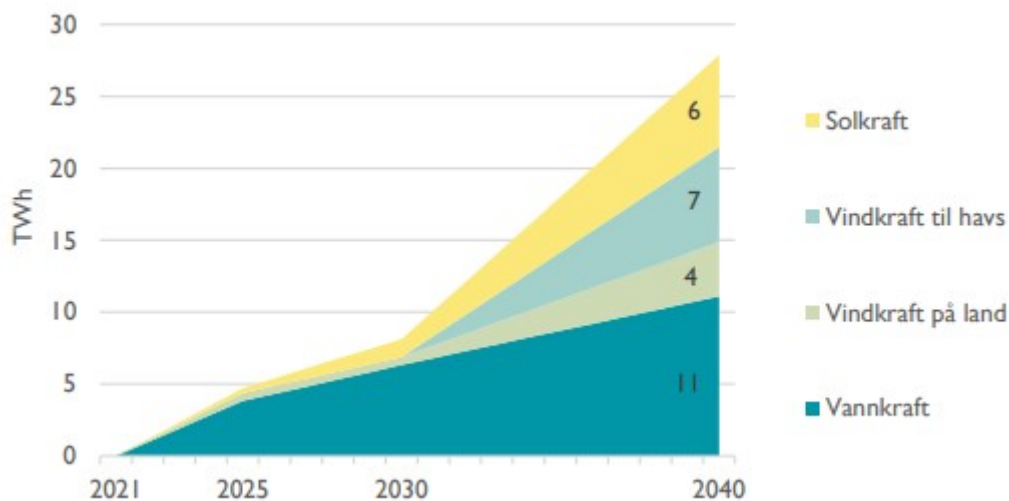
Figure 1.1: Forecast power production by different renewable sources in Norway. The top, yellow part shows the share of solar power.[1]

Bifacial PV is the fastest growing PV technology due to its higher energy density, caused by the absorption of radiation on both sides of the panel, and the ever-decreasing prices.[7] Unfortunately, there is little research on the performance of bifacial PV in the Nordic climate. This includes the best panel configurations for different energy consumption and modelling of bifacial PV in the Nordics. Most of the work on the topic is based on simulation or conducted in the South-Eastern part of Norway.[8][9][10] More literature on the topic is provided in Section 2.

1.2 Aim and scope of the work

The goal of this thesis is to provide real data on bifacial systems in Trondheim, Norway (63.42° N, 10.40° E) and to find the optimal configuration for the bifacial panels at this latitude. Furthermore, the measured data are compared with the simulated results using two different commercial software commonly used in the PV industry, called PV*SOL and PVsyst. The aim is to evaluate the software for the different bifacial configurations and to find the best software to use at high latitudes. Additionally, the options of sky models in the software are evaluated with regard to the configurations and climate.

The measured data will be collected from a bifacial PV laboratory placed on the roof of a fourteen-story high building called Sentralbygg 1, located on campus Gløshaugen at NTNU. Here, four different configurations are set up, the first having a fixed tilt of 44°toward the South. The next two are vertical, one facing East/West, and the other facing South/North. The last is a two-axis tracking system that follows the Sun throughout the day.

1.3 Previous work

A project thesis, which is the pre-work leading up to this master thesis, was conducted in the Autumn of 2021. The project evaluated the energy production of different bifacial and monofacial systems located at campus Gløshaugen in Trondheim, Norway, one of them being the same system with the same configurations as in this thesis.

The project found the bifacial gain to be highly dependent on the amount of direct radiation, as well as albedo, and the amount of light reaching the ground of the rear side of the panels. The results showed a bifacial gain of - 5% in October and + 12% in November. However, these results were based on data from two different systems with different cite-specifics and did not yield a valid result. The best fixed configuration for October was the 44°tilt, while the vertical S/N configuration was the best in November. The energy produced by the different configurations in the Alfa Centauri laboratory, which is a bifacial system further elaborated in the methodology section of this thesis, is seen in the table below. The values in parentheses are the energy production in the percentage of the energy production of the tracking system for each month.[4]

Table 1.1: The average energy production by the different sub-systems on Sentralbygg 1 for October and November. The numbers in parenthesis are the percentage of the sun-tracking production.[4]

Month	Vertical E/W	Vertical S/N	44°tilt South	Sun-tracking
October	5 051 Wh (61%)	7 135 Wh (86%)	7 477 Wh (90%)	8 308 Wh
November	2 535 Wh (33%)	7 454 Wh (96%)	5 624 Wh (72%)	7 793 Wh

2 Theory and Literature

This chapter presents the relevant theory and literature to understand the latter parts of the thesis. It discusses the characteristics and principles of solar cells and photovoltaic modules, the components of irradiance and how to model it, and important research on bifacial PV.

2.1 Silicon Solar Cells

A solar cell is a device that converts light into electricity. The device consists, most commonly, of a thin silicon wafer doped with boron or phosphorus, making it a conductive material.[11] When the cell is illuminated, light is absorbed and electrons excite from the valence band to the conduction band of the solar cell; see Figure 2.1 for an illustration. For this to happen, the energy of the photon, E_{ph}, must be equal to or greater than the band gap energy, E_g. Semiconductors like silicon have an intermediate-sized band gap, which is suitable for solar irradiance and, therefore, is excellent for solar cells. For solar panels, band gaps between 1.3 and 1.5 eV yield the highest efficiency.[12]
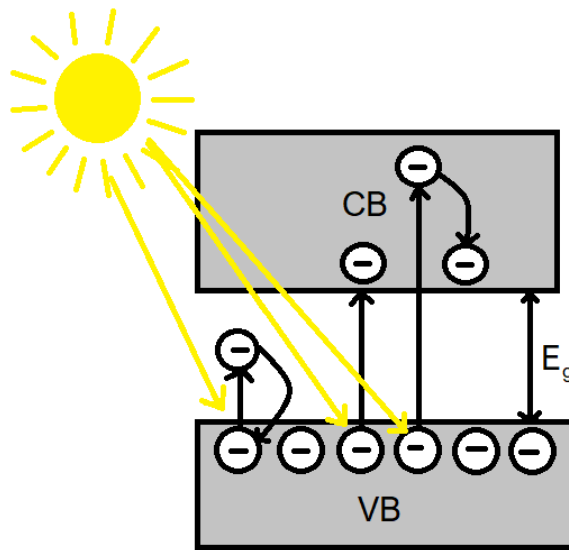
Figure 2.1: Electrons excite from the valence band to the conduction band only if the energy of the photon is greater than the band gap energy.

In 2020, 95% of the photovoltaic production was based on silicon wafers, whereas 85% was monocrystalline technology. Making monocrystalline silicon is a more energy intensive process than making multicrystalline silicon, but in return, the result is higher grade silicon and thus higher efficiency silicon solar cell.[13] Over the last decade, the efficiency of commercial wafer-based silicon modules has increased from around 15% to more than 20%, where the record lab cell efficiency is 26.7% for monocrystalline and 24.4% for multicrystalline.[14]

2.1.1 Bifacial and Monofacial solar panels

The share of bifacial solar cells is increasing in the market as more research is conducted in the field. Bifacial panels can absorb solar radiation from both the front side and the rear side, whereas monofacial panels absorb only solar radiation from the front side. A bifacial panel can produce up to 30% more energy than the same sized monofacial panel; hence, it will produce more energy at lower material and area usage.[7] Bifacial panels are slightly more expensive than monofacial panels, but the higher energy yield still makes them more cost effective.[15]

Bifacial panels have metal contacts and a transparent back sheet on the rear side, which allows light to be absorbed on this side, while monofacial panels have an opaque back surface foil, usually made of aluminium.[16][17] See Figure 2.2 for an illustration of the two technologies.
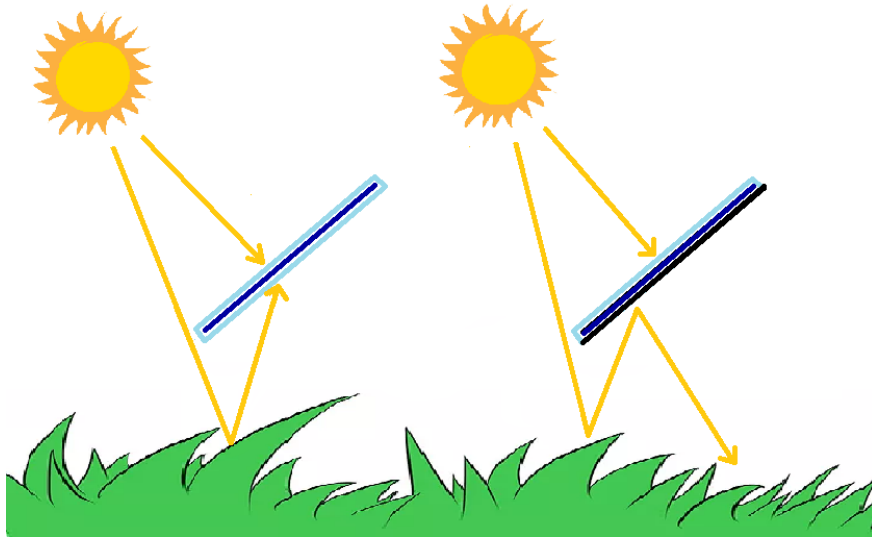
Figure 2.2: Illustration of the basic difference between a bifacial panel, on the left, and a monofacial panel, to the right.

2.2 Bifacial Photovoltaics

The gain of a bifacial system versus a monofacial system depends on the design of the system and the condition of the environment. The bifaciality of the panel and external factors like the albedo and mounting details play a great role when optimising a bifacial system.[18]

2.2.1 Bifacial gain

The additional energy delivered by bifacial PV panels compared to monofacial panels is called bifacial gain (BG). This is one of the most important parameters when discussing bifacial solar panels, and finding the optimum configurations for bifacial panels to maximise this gain is important.[19] However, it is not a module property, but a factor that depends on the location, radiation and angle of the module. The bifacial gain is given by Equation 2.1 where $E_{bifacial}$ is the energy yield of a bifacial panel and E_{mono} is the energy yield of a monofacial panel.

$$BG_E = \frac{E_{bifacial}}{E_{mono}} - 1 \tag{2.1}$$

The BG depends on the surface irradiation hitting the rear side of the panel. This is again dependent on factors like the albedo, which is how much light is reflected from the ground, and the mounting structure and geometry. Especially important here is the height of the panels, the tilt angle of the panels, and the row-to-row distances. Minimising the amount of shading on the front side is important, but minimising shading on the rear side is also important for bifacial panels.[19]
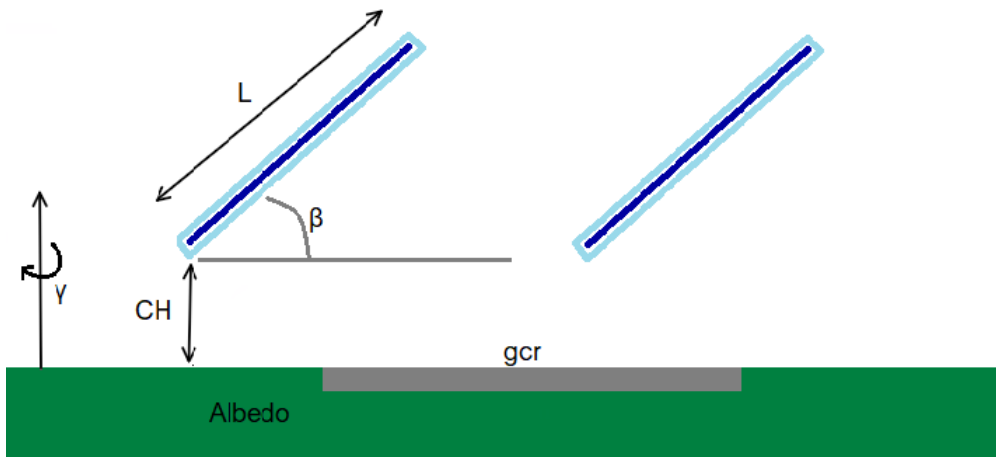
Figure 2.3: Factors influencing bifacial gain.

Figure 2.3 shows some important factors that influence the bifacial gain. Here, CH is the clearance height, which is the height from the ground to the bottom of the panel. γ is the azimuth angle, L is the length of the panel, β is the angle of inclination, and gcr is the ground coverage ratio, which describes the ratio of the module area to the area of the array. That is, how large a proportion of the system area that collects radiation.

2.2.2 Bifaciality

The bifaciality factor is a module property that is defined as the ratio of the efficiencies of the front and rear sides when illuminated separately.[7] It is given by Equation 2.2, where η_{front} and η_{rear} are the efficiency of the front and rear sides, respectively.

$$\text{Bifaciality factor} = \left[\frac{\eta_{front}}{\eta_{rear}}\right] \cdot 100\% \tag{2.2}$$

2.2.3 Climate

The climate is very important to consider when installing PV modules. The most important factor is, of course, radiation, and how much sun the location has, but vegetation such as mountains and latitude also play a great role. The location of this thesis is Trondheim, which is 63,4°North and 10,4°East and has a coastal Nordic climate. The Nordic climate is characterised by long and mild days in the summer and cold and short days in the winter, sometimes with snow. The climate in Norway has large variations mainly due to topography. Norway has deep valleys and high mountains with more extreme weather, while other places are more stable and have a more flat landscape.[20] Either way, the largest share of the total solar radiation in Norway is available during the summer. At mid-summer in Trondheim, the Sun is 50 °above the horizon at the highest, and at midwinter, it is 3.3° above the horizon at the highest. This makes it difficult to find a fixed optimum angle for solar panels.[21] Also, Trondheim has a lot of cloudy days, with little direct radiation, another challenge for this location.

As low temperatures are ideal for solar cells, the Nordic climate is ideal. However, the low radiation is a more challenging aspect. Multiple simulation studies suggest that bifacial PV systems are beneficial in northern latitudes. A vertical system is especially beneficial in terms of less soiling when it comes to snow and the low sun in the winter. According to S.Guo et al. East-West vertically mounted bifacial solar cells have higher performance than conventional monofacial modules facing the South in a Nordic climate.[22] Another study shows the equivalent performance of vertically bifacial panels facing East-West and South-North and suggests that a combination of the two is optimal for high latitude places.[9] Both of these studies are based on modelling, not real data from actual solar panels.

2.2.4 Shading

Mismatch losses due to shading are one of the main issues in PV modules and occur if the electrical parameters of one solar cell are different from the other cells in the same module. The output of the module is determined by the solar cell with the lowest output; therefore, if one cell is shaded, then the whole module will not produce any power. It can also be caused by circuit configuration and cell manufacturing differences. The mismatch can lead to local power dissipation, which can cause damage to the module. This results in local overheating and is called hot spot formation, which can again lead to cell degradation or the destruction of panels.[23]

The effect of shading on monofacial PV systems is mainly a result of the surrounding vegetation and buildings, which is an increasing issue due to urban densification. These parameters also influence the bifacial PV, but in addition, self-shading on the rear side is an important parameter to minimise.

The irradiance hitting the rear side is inhomogeneous, usually caused by self-shading. The PV

modules cause shade on the ground, decreasing the amount of light reflected. This is affected by the mounting height, the tilt angle, the module length, and the ground coverage ratio. Additionally, the support structure, albedo, and azimuth angle influence how much of the rear side is covered in shade.[24] [25]

By implementing an albedo of 0.5 compared to 0.25 and lifting modules 1 m above the ground surface compared to a ground mounted system, the bifacial gain can potentially be enhanced by up to 30%.[10] The rear-side irradiation increases with a higher installation height, as self-shading comes primarily from the module itself when the module elevation is zero.[26]

2.2.5 Optimal tilt angle

The optimal tilt angle for a bifacial PV can differ from the optimal tilt angle for a monofacial panel due to the need to optimise the radiation hitting both surfaces. A PV panel produces the most energy when the sunbeams are perpendicular to the panel. A way to utilise this is with a two-axis tracking system. These systems track the Sun throughout the day and move in both a vertical and a horizontal direction. These systems are very expensive and rarely used in solar parks due to price, so finding an optimal configuration is of great interest to the photovoltaic industry.[27]

The optimum configuration will depend on latitude, day of the year, and time of the day. A general rule of thumb in the PV industry is that the optimal inclination angle of the panel is the same as the latitude of the place in which it is placed and orientated in the direction of the equator. However, this rule is not valid for very high or very low latitude places where the radiation and the Sun's position vary to a large degree through the different seasons.[27] This is the situation for Trondheim, which is 64°North.

Based on the PV * SOLs optimisation tool, the optimal inclination angle for a bifacial panel in Trondheim, Norway is 44°facing South. Results from Rodrigez et al. reveal that for latitudes above 40°, any orientation of bifacial modules is more cost-effective than any orientation of monofacial modules.[28]

An article from Hannover, Germany, by Mubarak et al. shows that a fixed South configuration will yield the highest yearly energy output, but an East/West or a South-East/South-West configuration will reduce the cost of storing the energy and, as energy prices continue to increase, also reduce the electricity costs. These configurations produce about 5-6% less energy than the fixed South configuration, but since they produce energy over a longer time span, they are economically beneficial.[29]

2.3   The characteristics of a solar cell

When a solar cell is not illuminated, it has the same electrical characteristics as a diode. When the cell is illuminated, the curve shifts, where the distance of the shift depends on the light intensity. The greater the intensity, the greater the shift. In the end, the distance of the shift equals the short-circuit current. Unlike a diode, the convention for solar cells flips the curve. [13] The IV curve in Figure 2.4 shows an IV curve, where the different parameters presented will be explained in more detail in this section.
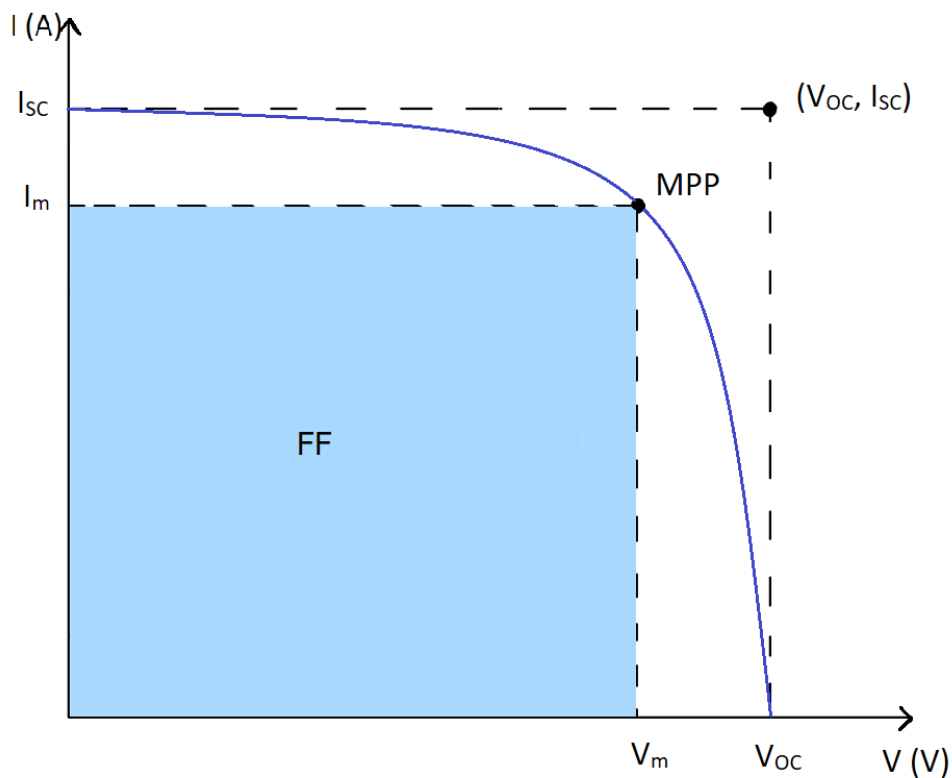
Figure 2.4: The IV curve of a solar cell illustrates the characteristic parameters.

2.3.1   Standard Test Conditions (STC)

Since the external parameters of photovoltaic panels greatly influence the output, photovoltaic manufacturers rate the power output of the panels after manufacturing them with a flash test under Standard test conditions (STC). In this way, it is possible to compare different PV technologies.

STC are defined by three parameters. The light that hits the panel has an irradiance of 1000 W/m^2, air mass (AM) is 1.5, and the temperature is 25 ° C. The power output is usually reported in W or Wp (watt peak) and is the maximum power point a panel can achieve. [30]

2.3.2 Short circuit current

The short circuit current, I_{SC}, of a solar cell is the maximum current that can be produced when the voltage across the cell is zero, as can be seen in Figure 2.4.

The short-circuit current depends on the incident light and the diffusion of electrons and holes in the cell. Furthermore, the optical properties of the cell, such as light absorption and reflection, as well as the area of the cell.[13]

The equation for I_{SC} is approximated in Equation 2.3 where q is the electronic charge, A is the area of the cell, G is the generation rate, L_e is the diffusion length of electrons and L_h the diffusion length of holes.[31]

$$I_{SC} = qAG(L_e + L_h) \tag{2.3}$$

The band gap energy decreases with increasing temperatures, which again increases the electron-hole pair generation, and thus increases the short-circuit current. However, this change is very small, usually around 0.05-0.07% per °C for silicon solar cells.[30]

2.3.3 Open circuit voltage

The open circuit voltage, V_{OC}, is the maximum voltage that can be produced from a cell when the current is zero. As can be seen in Figure 2.4, V_{OC} is where the IV curve intersects the x axis. Equation 2.4 shows the equation for V_{OC}, where k is the Boltzmann constant, T is the temperature in Kelvin, and I_0 is the dark saturation current and is given by Equation 2.5.

$$V_{OC} = \frac{kT}{q} \ln\left(\frac{I_{SC}}{I_0} + 1\right) \tag{2.4}$$

$$I_0 = 1.5 \cdot 10^5 \exp\left(-\frac{E_g}{kT}\right) \tag{2.5}$$

Here, E_g is the energy of the band gap. This temperature dependence has a stronger effect on the open-circuit voltage than on the short-circuit current. A temperature increase results in a decrease in the voltage.[13]

2.3.4 Maximum power point, MPP

The maximum power point, MPP, of a solar cell is the maximum power that can be extracted from a cell and is given by Equation 2.6. Here I_m and V_m are the maximum current and voltage, respectively.

$$P_{MP} = V_m I_m \tag{2.6}$$

In Figure 2.4 the MPP is located at the bend of the IV curve given by the I_m and V_m. I_m and V_m can be estimated from V_{OC} and I_{SC}:

$$V_M \sim (0.75 - 0.9)V_{OC}$$
$$I_M \sim (0.85 - 0.95)I_{SC}$$

Cell voltage and current depend on temperature, which means that the supplied power also changes with temperature. The power of crystalline silicon solar cells drops by about 0.4–0.5%/°C.[30]

2.3.5 Fill Factor, FF

The fill factor (FF) describes how close the IV curve is to the ideal rectangle form. It determines the maximum power of a solar cell and is defined by Equation 2.7.[30]

$$FF = \frac{I_m V_m}{I_{SC} V_{OC}} \tag{2.7}$$

The fill factor is the largest area that can fit into the IV curve, which in Figure 2.4 is the area of the smallest dotted rectangle with length V_m and height I_m.[31]

2.3.6 Efficiency

The efficiency,η, is the ratio of the electrical energy output to the solar radiation input and is given by Equation 2.8.

$$\eta = \frac{I_{SC} V_{OC} FF}{P_S}, \tag{2.8}$$

where P_S is the input power from the sun, I_{SC} is the short circuit current,V_{OC} is the open-circuit voltage, and FF is the fill factor. The efficiency is measured by a flash test and given by the manufacturer as a way of comparing the performance of different solar cells with one another.[30] [31] The effect of the temperature on V_{OC} also affects the efficiency and the fill factor negatively, which results in poorer cell performance with increasing temperatures.[32]

2.3.7 NOCT

The nominal operating cell temperature, NOCT, is the cell temperature reached by I_{NOCT} and the ambient air temperature of 20 ° C. The determination of NOCT is important to predict the behaviour of the module under real operating conditions. NOCT varies with module design, material, and installation; for example, a stand-alone system and a roof-mounted system will experience a significant difference in operating temperature.[33]

2.4 Solar Radiation

Solar radiance is the intensity of solar electromagnetic radiation emitted by the Sun, while solar irradiance is the radiation received from the Sun per unit area, usually measured in Wh/m^2.[34] Solar irradiance varies due to absorption and scattering by the atmosphere, season, time of day, as well as local effects such as pollution. Scattering of light occurs when there is a non-direct or diffuse light, which means that it does not come directly from the source.[13]

The irradiance received by a surface consists of three components, namely direct radiation, diffuse radiation, and the albedo which is the reflected radiation from the surroundings.[34] By adding the different radiations we get the global radiation, I_g, given by Equation2.9, where I_b is direct radiation, I_d diffuse radiation, and I_a is the reflected radiation(albedo).

$$I_g = I_b + I_d + I_a \tag{2.9}$$

2.4.1 Angles

Figure 2.5 shows some important angles for the installation and modelling of PV systems[35]
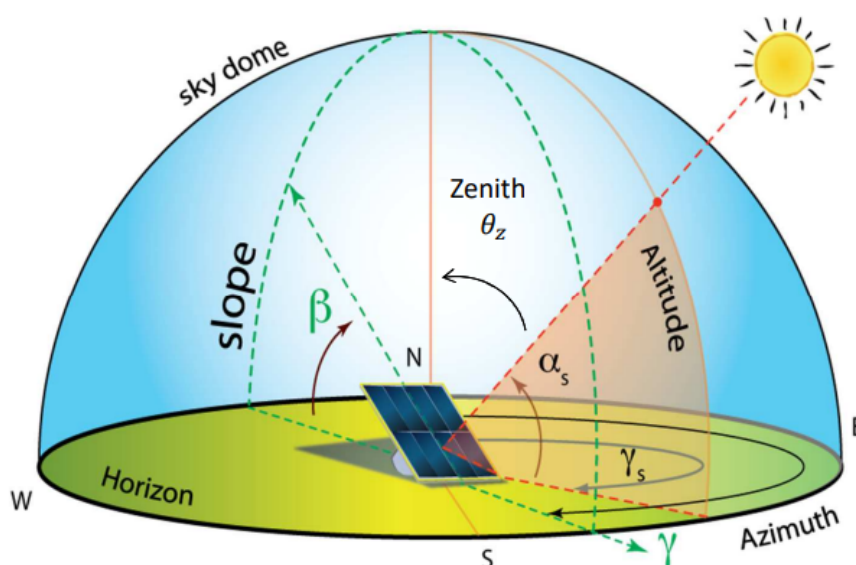
Figure 2.5: Some important angles for the installation of PV systems.[2]

α_s is the elevation angle, which is the angle between the horizon and solar radiation. This angle will vary throughout the day. γ is the azimuth angle which is the angle measured clockwise from North around the panel's horizon. In other words, it is the celestial direction in which the panel is facing. If it faces South, the azimuth angle is 180°. The zenith angle, θ_z, is the angle between the sunbeam and the vertical, this means that the zenith angle is 90°- α_s. Lastly, the tilt angle, β, or inclination angle, is the angle between the surface of the panel and the horizon.[36]

2.4.2   Measurements of solar radiation

Most weather stations measure global horizontal irradiance (GHI). This is measured by a pyranometer, which is placed horizontally to the ground and measures all radiation received from above. Due to more advanced and expensive equipment, measuring direct normal irradiance (DNI) and DHI. DNI is the amount of solar radiation received by a surface perpendicular to the Sun's rays. This is measured by a pyrheliometer, which tracks the Sun throughout the day. DHI is the radiation received from the scattering radiation and thus is not direct radiation. Another tracking system is needed for this, and a pyranometer with a shadow ball, where the ball is blocking the sun, is usually used. The correlation between the three components is given by Equation 2.10.[37][38]

$$GHI = DNI \cdot cos(\theta_z) + DHI \tag{2.10}$$

On cloudy days, the DHI values are close to the GHI values, and on completely cloudy days, the DHI is equal to GHI. It is often of interest to quantify how much of the radiation is diffuse. This is called the diffuse fraction and is given by Equation 2.11.[37]

$$Diffuse\ fraction = \frac{DHI}{GHI} \tag{2.11}$$

2.4.3   Air Mass

The AM is the path length through which light travels compared to when the Sun is at zenith (directly overhead). It is a way to quantify the attenuation of light by the atmosphere and is given by Equation. 2.12

$$AM = \frac{1}{cos(\theta_s)} \tag{2.12}$$

where θ_s is the zenith angle.[13]

Outside the atmosphere, the air mass is 0, and when the Sun is at zenith (directly overhead), the air mass is 1. At midsummer in Trondheim, the Sun is 50 °above the horizon at the highest,

and at midwinter, it isis 3.3° above the horizon at the highest. This results in an AM of 1.3 and 17, respectively.[39] An AM of 1.5 means that the Sun position is 1.5 times longer than if the panel were outside the atmosphere and is the STC when testing panels.[30]

2.4.4 Albedo

Albedo is a relationship between the light reflected from the ground and the total incoming light. It is a value between 0 and 1 and is a way of quantifying how well a surface reflects light.[40] Figure 2.6 shows the average albedo of the Earth, which is 30%, along with some common albedo values for different surfaces. Snow is highly reflective, resulting in a high albedo between 80% and 95%.[3]
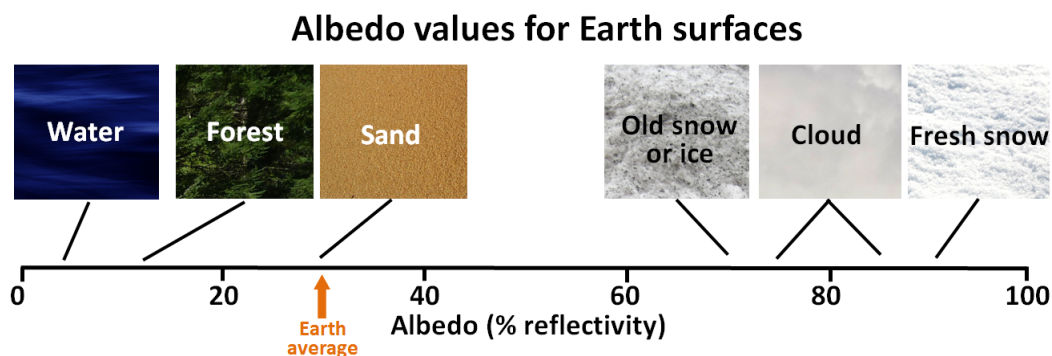
Figure 2.6: Common albedo values for different materials.[3]

For bifacial panels, the albedo is an important parameter because of the great impact it has on the radiation received from the rear side of the panel, especially if the panels are tilted. Therefore, placing bifacial panels somewhere with high albedo could take advantage of the fact that the panel is bifacial and thus result in a higher energy yield.[41]

The value of albedo changes throughout the day and season. This makes it difficult to model the light reflected from the ground. Since the bifacial gain is highly dependent on albedo, it is of great interest to have accurate measures of the albedo.[42]

Based on modelling, Sun et al. suggest that increasing the albedo of the ground to 0.5 with an elevation of the panels 1 m above the ground can increase the bifacial gain to 30%.[10] Calculations based on real data for panels mounted 0.3 m above the ground increase the BG from 6% to 11% when increasing the albedo from 0.2 to 0.4.[43]

2.5 Diffuse radiation models

Since most weather stations do not record diffuse horizontal irradiance, many models have been developed to predict realistic DHI. In this section, different decomposition models are briefly presented, including their characteristics. Most models are based on the Liu and Jordan model, which is presented first and will include some of the mathematical expressions. The selected

models are also models that are used in PV*SOL and PVsyst, which is the software used for simulations in this thesis.

2.5.1 Liu and Jordan model

This model is the mother of most other diffuse models and was made by Lui and Jordan and was published in 1960. The model is an isotropic sky model, which is based on the assumption that the sky is uniform in composition across the sky dome. This model, along with most other models, estimates diffuse radiation based on empirical observations of K, which is the diffuse fraction, and K_T, which is the clearness index defined in Equation 2.13 and 2.14, where G_{ext} is extraterrestrial radiation, which is the intensity of the Sun outside the atmosphere. [44]

$$K = \frac{DHI}{GHI} \tag{2.13}$$

$$K_T = \frac{GHI}{G_{ext}} \tag{2.14}$$

The paper suggests different values of K for a number of values of K_T, but no model is provided. After digitalising the figures in the paper, the following correlation was obtained:

$$K = 1 + 0.006381K_T - 3.2315K_T^2 + 2.2448K_T^3 + 0.081882K_T^4, K_t \le 0.75 \tag{2.15}$$

$$K = 0.16, K_T \le 0.75 \tag{2.16}$$

The model is based on daily totals of global irradiance, where later research has shown that the model does not function well in areas much different from where it was developed. Especially changes in elevation and albedo put the model off. [45]

2.5.2 Orgill and Hollands

The model presented by Orgill and Hollands is based on four years of hourly measurements from Toronto and was published in 1977. This was one of the first models to calculate DHI based on hourly measurements, rather than daily totals like that in Lui's model. The model suggests that 3 different correlations for K should be used for different values of K_T. Orgill and Hollands expect the model presented to accurately represent the radiation insolation between the latitudes of 43 ° N and 54 ° N[46]

2.5.3 Erbs, Klein and Duffie

The study by Erbs, Klein and Duffie was published in 1981 and is a further development of the relationship between the hourly diffuse fraction and the hourly clearness index, which Orgill

and Hollands presented. The model is based on four different cities in the US and develops a seasonally dependent daily diffuse correlation. The seasonal dependence takes into account that the air is drier in the winter, and thus the atmosphere scatters less radiation.[47]

2.5.4 Reindl reduced

Reindl's model is yet another development of the diffuse fraction, but this model studies the influence of climatic and geometric variables, such as the solar altitude, ambient temperature, and relative humidity, in addition to the clearness index. This model does not take seasonal dependence into account but shows greater errors in the fall and winter than on an annual basis. It was published in 1990 and is based on data from five different European and North American locations. Compared to previous models, this is an anisotropic model, which presumes that the sky near the solar disk, the circumsolar region, is anisotropic and the rest of the sky is isotropic.[48]

2.5.5 Perez and Ineichen

Perez has published several models, but the one presented in a paper from 1992 is presented here, which is one of the models chosen by PV*SOL. This is a new model compared to the previously mentioned ones and computes the direct irradiance from the global irradiance. Unlike the other models, it only records DNI measurements, not DHI. This is a more intricate anisotropic model, which uses solar zenith angle, the clearness index, dew point temperature as well as a variability index. The paper claims that the model is suitable for areas where intermediate sky conditions are frequent.[49]

2.5.6 Skartveit

Skartveit published a model in 1998, which, like Perez, has four input parameters. These are the hourly solar elevation, the clearness index, an hour-to-hour variability index, and the regional surface albedo. The variability index is the root mean squared deviation between the clear sky index of the respective hour, the hour before and the succeeding hour. The model also eliminates high normal beam irradiances at low solar elevations, which potentially removes errors at low solar elevations. Furthermore, it is based on 32 years of climate data from Bergen, Norway (60.3913° N, 5.3221° E).[50]

2.5.7 Boland, Ridley and Laurent

The model developed by Boland, Ridley and Laurent, BRL from now, is the only one of the presented models, which is developed in the southern hemisphere. Most diffuse models are developed in Europe or North America and do not adequately compute diffuse irradiance. The main motivation was to develop a model for Australian conditions. The paper was published in 2010 and the model was developed mainly for Australian conditions but showed good or better

results for multiple European places as well. The model is also a multiple predictor model, but simpler than the previous models. It uses an hourly clearness index, a daily clearness index, a solar altitude, apparent solar time, and a measure of the persistence of global radiation level. [51]

2.5.8 Hofmann

This model was developed by Hofmann for Valentine Software, which is a developer of PV*SOL. This model is the newest of the presented, published in 2017, and as opposed to the other models presented, this uses one-minute time series of global irradiance and geographical information. The model expresses the clearness index as probability matrices, instead of functions, to obtain a more realistic diffuse fraction. Furthermore, it introduces a minimum daily diffuse fraction and was compared to Perez's and Reindl's model for 28 locations around the world, where it was found to perform substantially better. [52]

Numerous articles exist on the analysis and validation of different decomposition models, but few in the Nordic climate. The ones that are conducted on the Nordic climate do not include the models presented in this thesis, or these models show too poor performance for them to even be presented. Overall, decomposition models perform better under overcast or clear sky conditions, while partly cloud cover is harder to model. [53] An article by Gueymard et al. mentioned Perez to show low deviations, but no consistency for tempered climates. Tempered climates are mild climates typical for locations in Central Europe. [54] Most of the locations where models are evaluated are below the latitude of 50°or in a polar climate, usually in a latitude above 70 °, and the newer analysis focuses mainly on newer models. [55]

2.6 Transposition models

Transposition models calculate the irradiance in the plane of the module from GHI, DNI and DHI. In other words, the models transpose the horizontal values into the module plane.

Numerous models exist and this section will briefly go through the models that are options in PV*SOL and PVsyst but will not go into the depth of the models' mathematics.

2.6.1 Liu and Jordan

One of the first transposition models was presented by Liu and Jordan in 1960. This is an isotropic model and calculates the global tilted irradiance using equation 2.17, where β is the module angle. This is the only isotropic model of those presented in this thesis. [56]

$$GTI = \frac{3 + cos(2\beta)}{4} \cdot DHI \qquad (2.17)$$

2.6.2 Klucher

Klucher's model is based on the Liu and Jordan model and was published in 1979. Klucher found Liu's model to be good on overcast days but showed poorer results on partly overcast and clear sky days. This model takes into account circumsolar irradiation and horizon brightening and introduces a factor that includes the degree of cloud cover. [57]

2.6.3 Hay and Davies

Hay and Davies published their paper in 1980 assuming the disc of the Sun and the rest of the sky with isotropic diffuse radiation to be the two primary sources of sky diffuse radiation. These are both described by an anisotropy index, which represents the direct normal irradiance transmittance by the atmosphere. The model does not consider horizon brightening. [58]

2.6.4 Perez

Perez is a more complex model and divides diffuse radiation into three components, namely isotropic background radiation, circumsolar radiation, and horizon brightening. This was published in 1987 and is the most mathematically complicated model presented here. [59]

2.6.5 Reindl

Reindl published one of his models in 1990, this model is based on the model by Hay and Davies, which includes the horizon brightening. Reindl includes the fact that the intensity of diffuse radiation decreases with increasing overcast sky in his model. [60]

As for the decomposition models, the transposition models suffer from the lack of validation at high latitudes as well. A study based on various locations in the USA by Lave et al. shows that the Hay & Davies model had the lowest bias when not using measured DHI values for the simulation. [61] A more comprehensive study by Yang showed that Klucher, Hay& Davies, Reindl and Liu all achieve good results for the location of Oldenburg in Germany(53.15 ° N, 8.17 ° E). This is based on a fixed tilt of 45°towards the South. This paper also studied the models on a vertical configuration, where it showed that most transposition models struggled to perform for vertical surfaces. [62]

2.7 PV Software

This thesis will compare two types of commercial software well used in the PV industry, PV*sol and PVsyst. The software is built for analysing different aspects of PV installations. This section will go through how the two types of software compute rear-side radiation, the computation of the bifacial gain, and how they handle the climate data.

2.7.1 PV*SOL

In PV*SOL, bifacial PV modules are calculated by Equation 2.18, which calculates the increase in effective irradiation, $E_{effective}$, of bifacial modules compared to monofacial ones:

$$E_{effective} = E_{front} + E_{rear} \cdot BF \tag{2.18}$$

Here, E_{front} and E_{rear} are the irradiation on the front and rear sides, respectively, and BF is the bifaciality factor specific for the PV module. The calculation of this rear-side irradiation depends on the configuration of the modules. For vertical modules, the back-side irradiation is calculated in the same way as the front-side irradiation. For tilted modules, the rear side irradiation, E_{rear}, is given by Equation 2.19.[63]

$$E_{rear} = E_{rear,ground} + E_{rear,module} + E_{rear,diffuse} \tag{2.19}$$

Here, $E_{rear,ground}$ is the radiation the rear side receives from the ground, $E_{rear,module}$ is the light reflected from adjacent modules, and $E_{rear,diffuse}$ and the proportion of diffuse light reaching the rear side. The irradiance hitting both the front and rear sides is assumed to be isotropic, which means that the radiation has the same intensity in all directions.[63]

2.7.2 PVsyst

PVSyst simulates a bifacial system with view factors, which calculates the proportion of radiation that leaves surface A (the surroundings of the PV panel) that strikes surface B (the rear side of the bifacial panel). This can be done in two different ways in PVSyst. The first mode is "unlimited sheds" with a two-dimensional calculation that includes tools to understand the different contributions of irradiance. The other mode is "unlimited trackers" (horizontal axis) with a two-dimensional calculation that includes precalculation for several positions of the trackers.

The bifacial model in PVsyst is based on three assumptions:

- The diffuse irradiance is isotropic

- The re-emission of each point on the ground is isotropic, specified with an albedo factor.

- The one-diode model is applied on the additional irradiance hitting the rear side added to the front.

The irradiance on the back side will increase the power output of the global photovoltaic module. PVsyst adds the rear incident irradiance, weighted by the bifaciality factor, to the front incident irradiance during the simulation before computing power using the one-diode

model. PVSyst takes into account a mismatch loss factor to account for the non-uniformity of the rear side of the modules and its effect on the total string current. Because there is no model to estimate this mismatch loss factor, it is set to 10% by default and can be changed by the user.

2.7.3 Climate Data

The climate data in PV*SOL can be uploaded by the user or imported from MeteoNorm, which is also an option in PVSyst. For locations not included in the database, satellite data and adjacent meteorological stations are used to interpolate data for the specific location. [64]

The climate data generated usually take periods between 10 and 30 years and compile a representative collection of days from these. This is called a typical meteorological year (TMY), which means that the generated hourly values are not an average over years because then the climate data would be washed out, but instead, they are chosen from a typical meteorological year. [65] This ensures that the data for a specific location are typical over the year, even though they could deviate from day to day. [63]

2.8 Accuracy measures

Relative root mean square deviation, rRMSD, and the relative mean bias deviation, rMBD, are two difference metrics widely used when comparing modelled values to measured ones. The rRMSD collects the magnitude of errors to predict the data. It focuses on the larger deviations in the model that are not systematic. The rMBD estimates the average bias in the model. It measures how much a model over or underestimates compared to the measured values. [66] [67] The equations for the two metrics are as follows:

$$rRMSD = \frac{\sqrt{\frac{1}{N}\sum_{i=1}^{N}(x_i - \hat{x}_i)^2}}{\sum_{i=1}^{N}\hat{x}_i} \tag{2.20}$$

$$rMBD = \frac{\frac{1}{N}\sum_{i=1}^{N}(x_i - \hat{x}_i)}{\sum_{i=1}^{N}\hat{x}_i} \tag{2.21}$$

3 Methodology

In this section, the photovoltaic system is described in detail and practical information regarding data recording and data analysis methods is introduced. Further, a thorough explanation of the modelling approach of the system in PV*SOL and PVsyst is presented.

3.1 The PV System

In this thesis, an outdoor solar cell laboratory called "Alfa Centauri" is being studied. The outdoor laboratory is brand new, installed in August 2021, and embraces brand new technology. The panels consist of 60 monocrystalline silicon PERC solar cells, each with an area of 240.8 cm². The modules are manufactured with a technology called New Industrial Cell Encapsulation (NICE), which does not laminate the panels, but has vacuum sealed glass on both sides for easier recycling.[68] "Alfa Centauri", which has status as a national infrastructure for solar cell research, is owned and operated by SINTEF.[69]

The PV system is located on top of a 14 story tall building called Sentralbygg 1 on the campus Gløshaugen at NTNU in Trondheim. Here four subsystems with two panels each are installed in a row 1 m above the ground, 6 m apart. The mounting structure is a pole placed in the middle of the two panels. Here, a small metal box is installed, which stores the measuring station for the panels. The subsystems can be arranged in a fixed orientation, or they can be programmed to track the Sun. This is called 2-axis tracking, where the system adjusts in both horizontal and vertical directions throughout the day.

Sentralbygg 1 is the highest building in the area, hence shading from other buildings or vegetation on the panels is not an issue. The floor is black and flat, and a railing is enclosing the roof, which is lower than the panels, so that there is no shading on the panels.

(a) The subsystems with different orientations.

(b) Close-up of a vertical panel.

Figure 3.1: Picture (a) and (b) show the Alfa Centauri photovoltaic laboratory.

Table 3.1: Characteristics of the PV panels

V_{OC}	40.4 V
I_{SC}	9.27 A
V_{MPP}	33.5 V
I_{MPP}	8.8 A
P_{MPP}	295 W
FF	78.9%
$Bifaciality$	65%
η_{front}	16.4%
η_{rear}	10.7%

3.2   Meteo Station

The meteo station shown in Figure 3.3, consists of two pyranometers, one for measuring global horizontal irradiance and one for measuring diffuse horizontal irradiance and one pyrheliometer. In addition to irradiance measuring devices, a thermometer for measuring ambient temperature, an anemometer used for measuring wind speed, a hygrometer for measuring relative humidity, and a rain gauge to measure the amount of precipitation. The datasheets for the different measuring devices can be found in Appendix A, including the uncertainties.
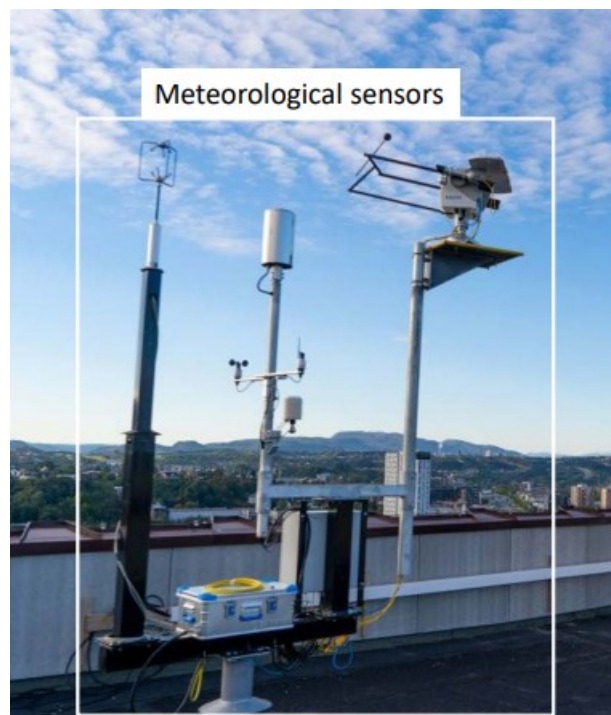
Figure 3.3: The meteo station on top of Sentralbygg 1 at campus Gløshaugen, NTNU.

3.3   The Setup

The four subsystems are set to 4 different configurations. The first system, which is farthest west, has a vertical South/North configuration. The next has a vertical East/West configuration. The third system has a fixed tilt at 44° toward the South (azimuth 180°/zenith 44°), while the last system has a two-axis tracking, which means that it will track the Sun throughout the day. The roof is black, with exceptions for days with snow. On days with a lot of wind, the panels are manually placed horizontally for security measures.

3.4   Data Recording and Analysis

Data from all panels and meteo data are recorded every day with a logging frequency of 10 seconds. The data are automatically uploaded to a website where they can be downloaded as text files. The data from the modules are in direct current (DC) since it does not power anything, but only for research purposes.

The files with data from the meteo station and the eight modules are processed and plotted in Python using the Matplotlib and Pandas packages.[70][71][72] Further, the data is analysed in terms of power and energy production, specific yield, and bifacial gain, as well as meteo data such as GHI and DHI. The meteo data is also processed for use in PV*SOL and PVsyst, which requires hourly data of GHI, wind speed, relative humidity, and ambient temperature.

3.5   Modelling in PV software

The system described above is simulated in both PVsyst and PV*sol, under the same conditions. A thorough description of the procedure of the modelling is presented in the following sections. In PV*SOL the system is modelled both in 2D and 3D since a sun-tracking system is not possible to model in 3D.

3.5.1   Meteo Data

Both software have multiple options for the use of climate data, as described below.

PV*SOL

Two types of meteo data were used and compared in the system simulation. First, there are the meteo data from Værnes, which is provided in PV*SOL. These data are based on 15 years of climate data and are provided by Meteonorm 8.1 as explained in Section 2.6.2. Værnes is located 35 km North of Trondheim.

The other meteo data is from the meteo station installed next to the modules on Sentralbygg 1. PV*SOL needs exactly 8760 values of climate data, which is exactly one value per hour for one year. Sine the meteo station has not been up for a whole year, the missing values are

Figure 3.4: The database of PV modules. PV modules can be added if they do not exist in the database, which is done in this thesis. This is done on the tab with the red circle around it.

replaced with the data from Værnes. The data recorded are averaged on the hour exported to DAT files to get the correct format.

PVsyst

The meteo data in PVsyst can be directly imported from Meteonorm, NREL NSRDB, which provides free satellite hourly data for the North and South Americas and India, or PVGIS which is also satellite data available for most places of the world. The other option is to import the data manually, where PVsyst also requires one value per hour. In addition to GHI, wind speed, relative humidity and ambient temperature, PVsyst allow the user to import data like DHI and DNI, but since this feature is not available in PV*SOL, these will neither be uploaded in PVsyst.

3.5.2 PV*SOL modelling in 3D

The system is modelled in 3D, with an exception for the tracking subsystem, since it is not an option in 3D to model tracking systems. Below is a step-by-step guide on how to model a system in PV*SOL 3D. A similar, but easier procedure is carried out in 2D, and will not be described in this section.

1. The PV modules and their characteristics like dimensions, bifaciality, etc. are done before the actual modelling in the database alternative.

2. The next step is to choose the meteo data. Either by using the database in PV*SOL, or importing measured climate data. In this thesis, both methods have been tested.
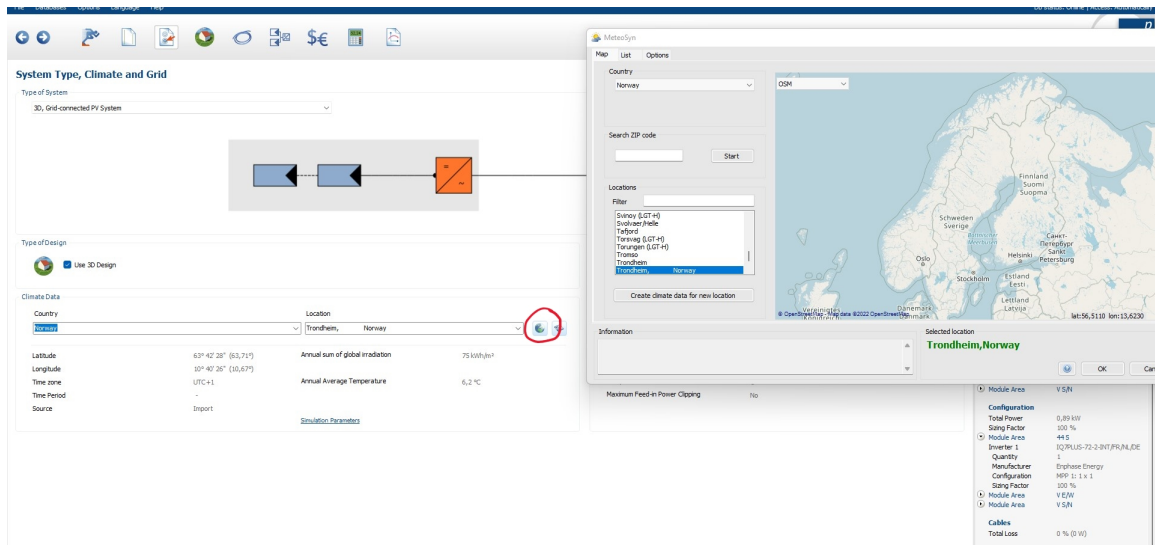
Figure 3.5: Choose or upload climate data.

3. Choose simulation parameters, like the diffuse model and transposition model, as well as a monthly or yearly albedo and monthly or yearly soiling coefficient.
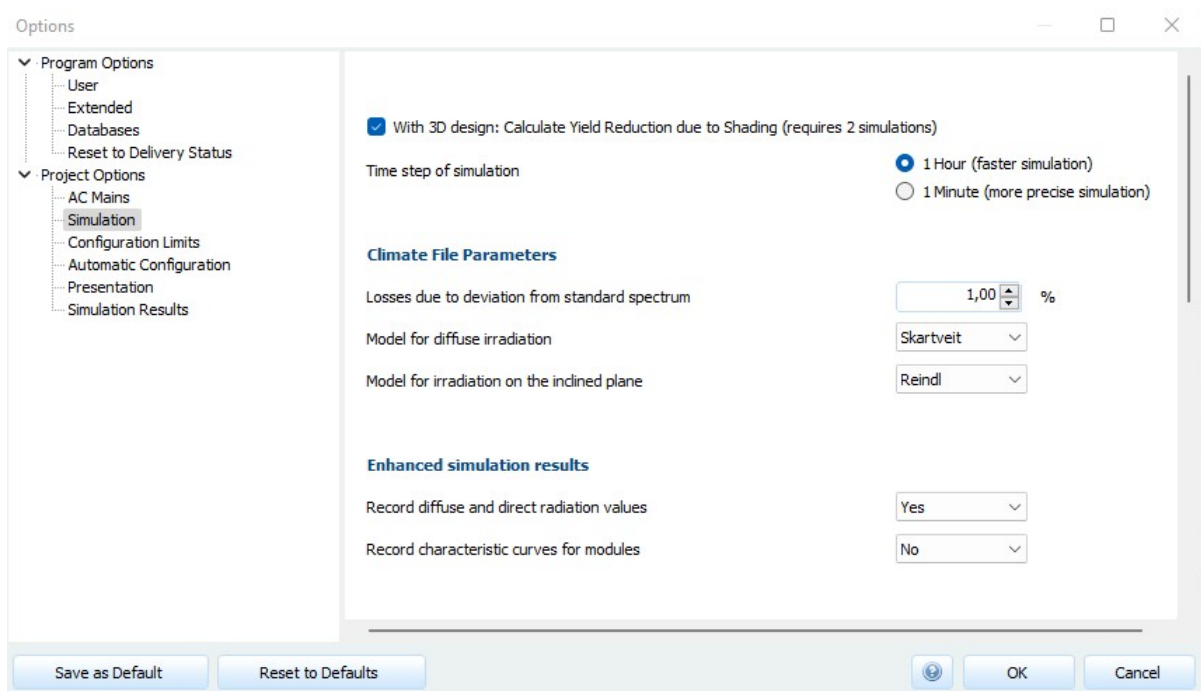
Figure 3.6: In this thesis, all the different diffuse models and transposition models have been tested. This is done in this tab called "Simulation Parameters", which is also where the albedo is set.

4. To build a 3D model, a picture of the location is needed. This can be fetched in Google Earth Pro, where the dimensions of buildings and objects that may cause shade on the modules can be measured. Valentine Software has an explanatory video guide on this, which can be found on their web page. In this case, it is Sentralbygg 1 with substructures

on top of it. Since there is no higher building or vegetation around this is the only building drawn.
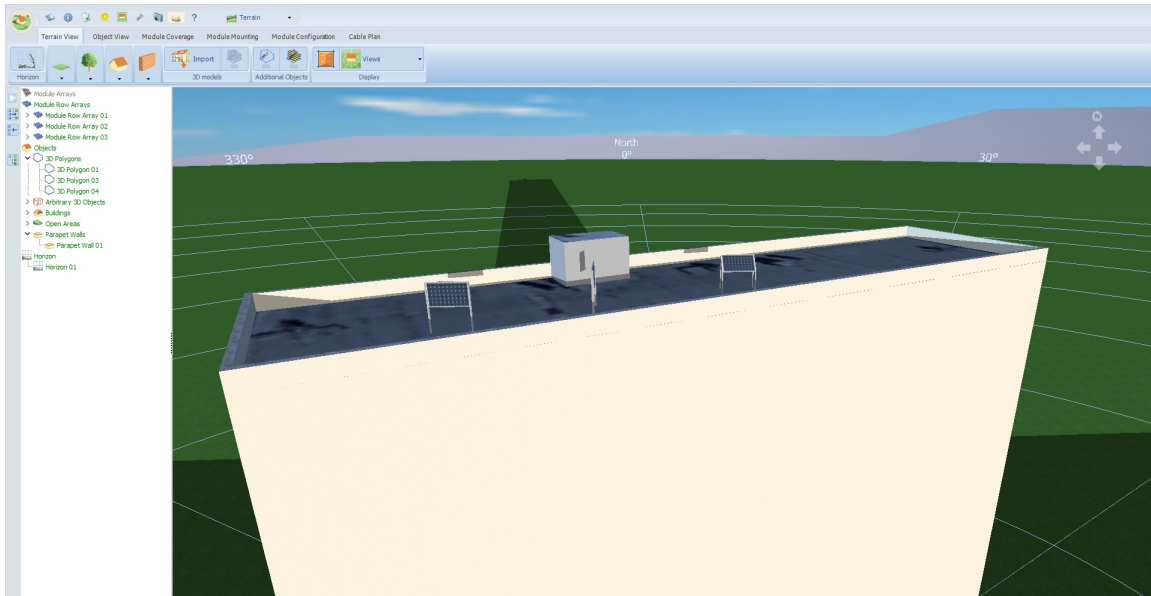
Figure 3.7: A snippet of the 3D animation tool in PV*SOL. Here, Sentralbygg 1 is drawn with substructures and modules on top.

5. The next step is to add the horizon. This can be done by choosing the exact location on a map. This will automatically add the horizon for this place based on data from PVGIS. The data can be edited, or measured data can be uploaded manually. For this project, the horizon generated by PV*SOL is used.
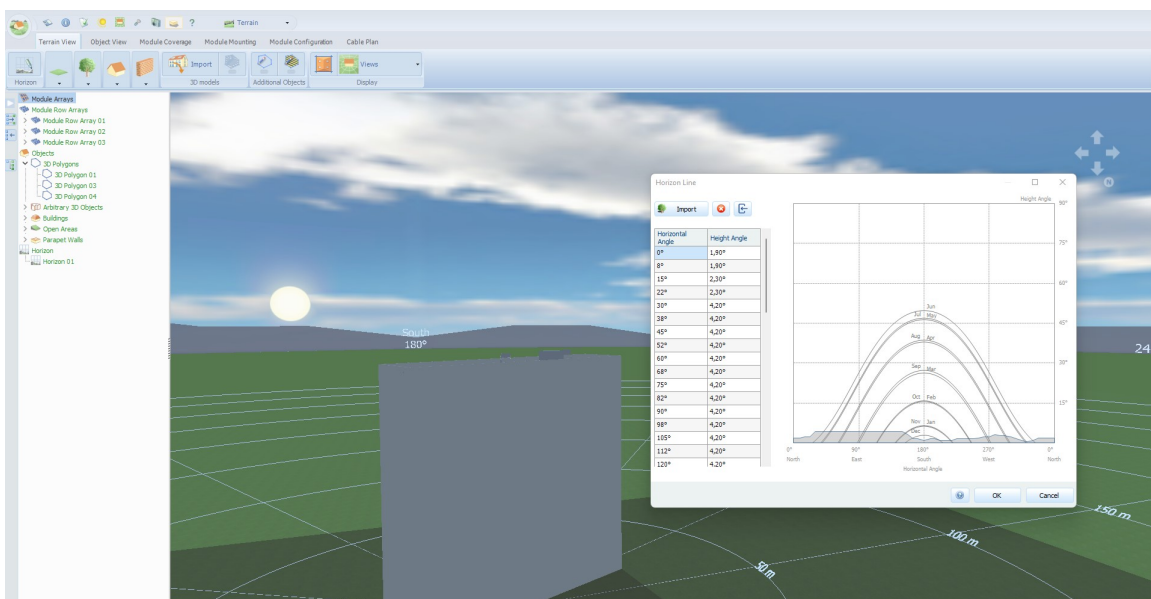
Figure 3.8: Horizon in PV*SOL

6. In the module mounting section, the type of PV modules is chosen as well as their configuration.

7. In the module configuration section, the inverter technology for the system is added. In this case, a mini inverter was chosen for each panel; since the system does not have an inverter, the same inverter was chosen in PVsyst.

8. Perform a shading simulation. This is the last step in the 3D editor.

9. Get the results.

3.5.3 PVsyst modelling in 2D

PVsyst has two options for modelling bifacial panels. One has to choose either "Unlimited sheds" or "Unlimited trackers". The latter can only model one-axis tracking, so the two-axis tracking system cannot be modelled in PVsyst. This section provides a step-by-step guide to modelling the three other subsystems in PVsyst.

1. Before starting the modelling, the climate data and the modules are added to the database. This step is similar to the first step for the simulation in PV*SOL.
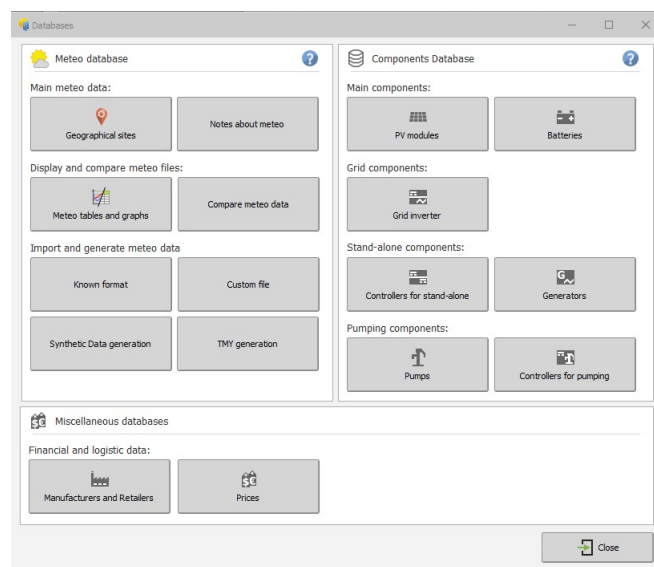
Figure 3.9: In this tab th climate data and PV modules are added to the database before starting the modelling.

2. The first step of the modelling is deciding the project name, site of the system and choosing the preferred meteo file.
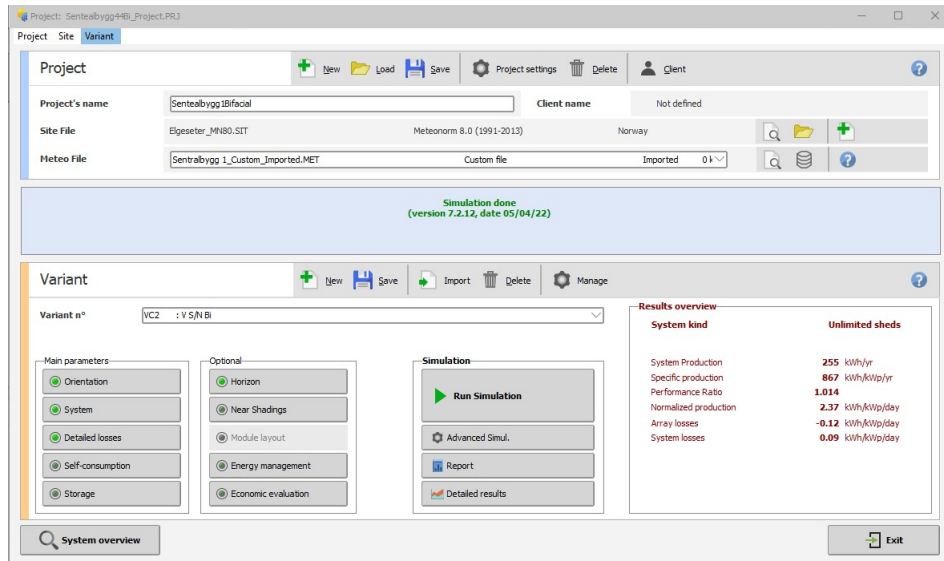
Figure 3.10: The user interface of the project. The first step is to decide on the location and meteo data.

3. In the orientation box, "unlimited sheds" or "unlimited tracking" are chosen for modelling of bifacial modules. Since the latter alternative only applies for one-axis tracking, the "unlimited sheds" alternative is chosen.
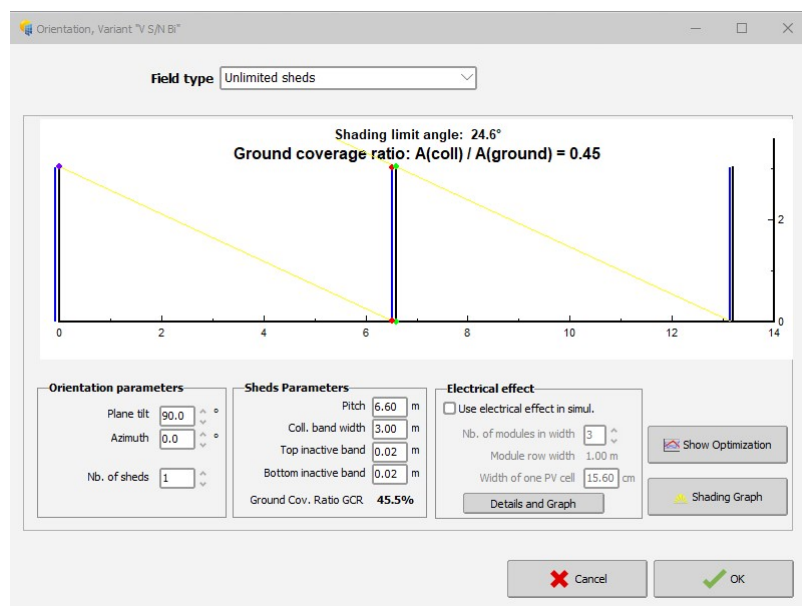
Figure 3.11: Unlimited sheds must be chosen in this tab for PVsyst to simulate bifacial panels.

4. In the "system" box, the bifacial panels are chosen as well as inverter technology. Here, the configurations of the bifacial panels are chosen by clicking the "Bifacial" button. The specifics of the panel configurations are decided here.
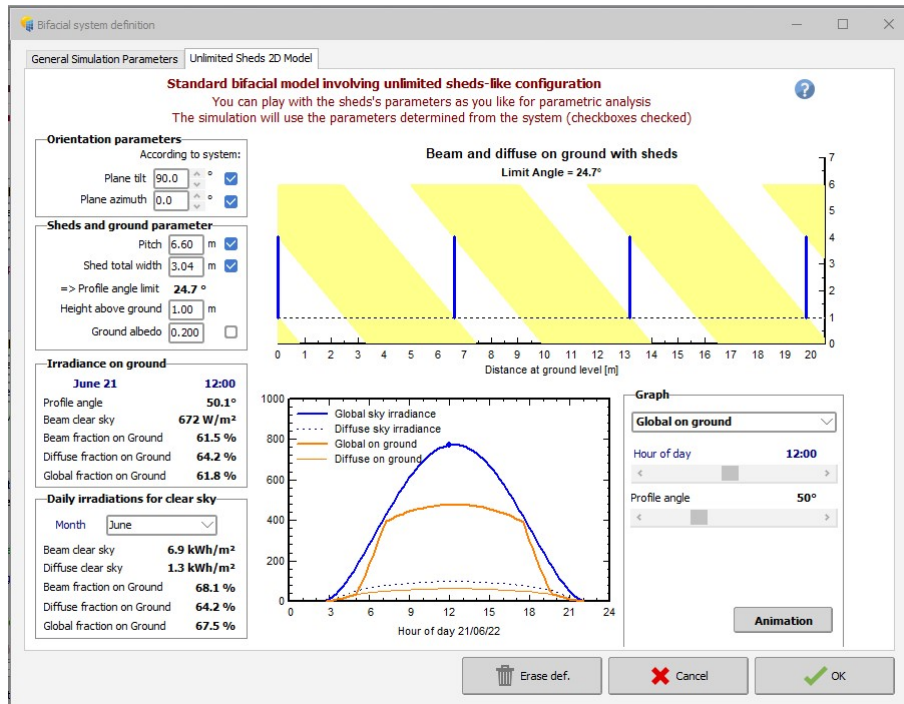
Figure 3.12: 2D animation of the bifacial unlimited sheds. Here, the height over the ground and albedo is decided.

5. The horizon is imported in the same manner as in PV*SOL.
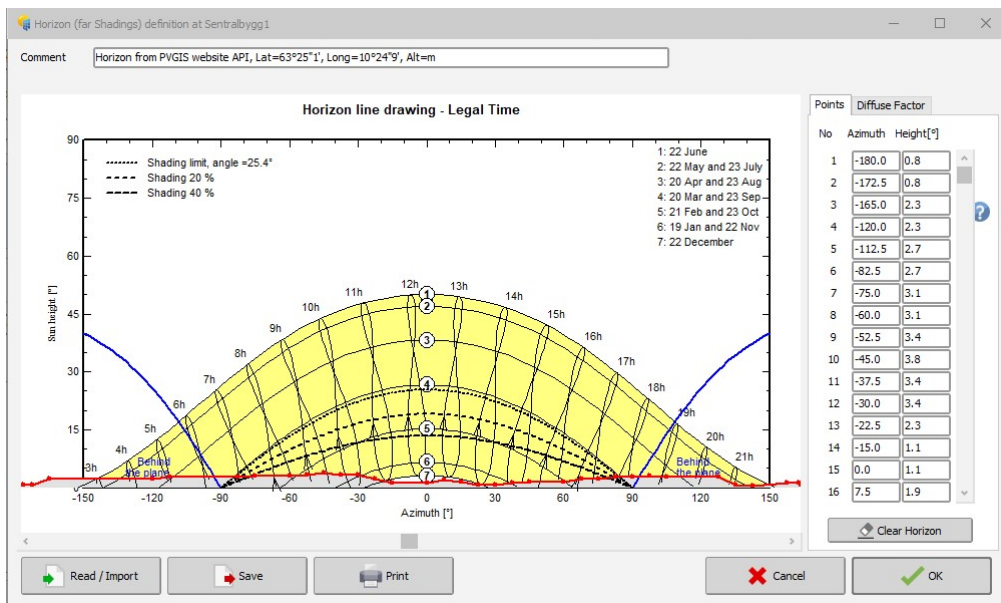
Figure 3.13: Importing the horizon in PVsyst works the same way as in PV*SOL.

6. The 3D simulating in the "near shadings" box is not utilised in this project.

7. Run an advanced simulation to get the output as a CSV file.

3.6 Plan for experiment

The original plan of this thesis was to measure the output of the four configurations explained in Section 3.3, and to cover one of the panels on one side with a black film, to quantify the bifacial gain throughout the semester. However, a panel fell down in December due to an installation error caused by the wrong use of a screw. This created a hole in the roof and a leakage, which had to be HSE assessed. The screw had to be ordered from China, which due to the war in Ukraine and the pandemic took a long time. The screw never made it in time for this thesis deadline, resulting in only a few months of data used in the project thesis, which was the preliminary project of this master thesis.

The plan was further to simulate the system in both PV*SOL and PVsyst, to see which of the two software is most suitable for modelling PV systems in Trondheim. Especially the winter months and the vertical configurations were of interest to see how well the software would simulate and match up with measured values. Because the panels were not mounted again after the accident, the simulated values were compared with the months of October and November. Because of this, it is also not possible to quantify a proper bifacial gain.

3.6.1 Energy production

The first part of the result of this thesis will focus on the energy production of the different configurations based on climate data provided by MeteoNorm. This helps decide which of the configuration the simulation tools recommend for Trondheim. This analysis will be based on a whole year. Next, an analysis of the accuracy of the simulation of the different configurations is performed. The energy output from PV*SOL 2D, 3D, and PVsyst for each configuration is compared to the measured values. In all of these cases, the DHI model used is Erbs and the transposition model used is Perez, in both software.

3.6.2 Investigation of DHI and transposition models

The other part of this thesis came along when it was clear that the modules would not be mounted in time for the finalisation of this thesis. This part goes deeper into the choice of sky models and is mainly focused on PV*SOL, which has the most options to choose between.

PV*SOL has seven different options for modelling diffuse horizontal irradiance, which is explained in Section 2.5. The simulation is carried out for each of these to find the best model for Trondheim, and which ones to avoid. Furthermore, the different transposition models combined with the DHI models are examined. Since there were no measurements of the irradiance in the plane of the module for the different configurations on Sentralbygg 1, the energy production is compared. PVSyst has only one decomposition model, but two transposition models to choose from, while PV*SOL has five transposition models and seven decomposition models, resulting in 35 different combinations available of sky models.

The last part of the thesis is a comparison of PV*SOL and PVsyst in general and will focus on the user interface and their options for bifacial modelling in Trondheim.

4 Results

4.1 Monthly results of energy production, modelled versus measured data

The monthly results are compared with the measured results for October and November based on simulations from PV*SOL 2D, PV*SOL 3D, and PVsyst. The climate data used is imported manually from Sentralbygg 1. To compare the two software, the same models for diffuse irradiance and transposition were used, namely, Erbs and Perez.
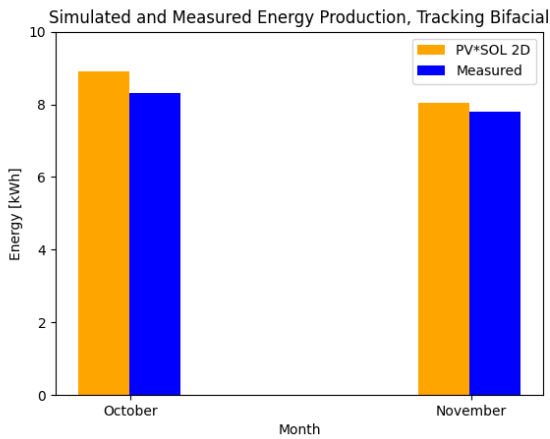
(a) Comparison for the two-axis tracking panel.
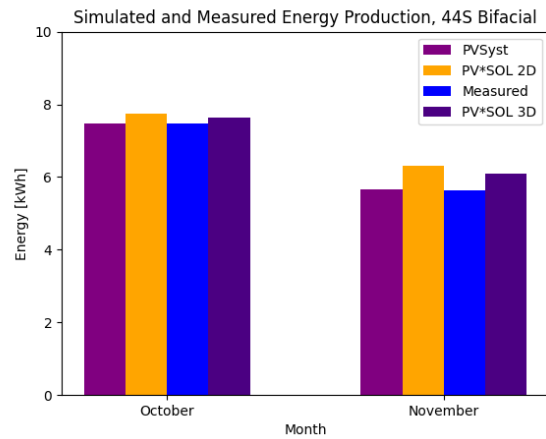
(b) Comparison for the panel facing South at a 44°tilt.
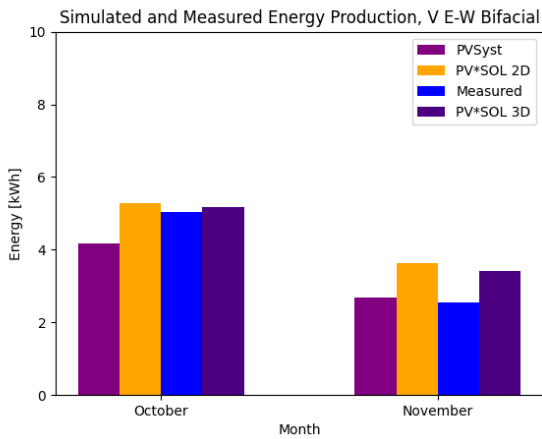
(c) Comparison for the vertical East/West panel
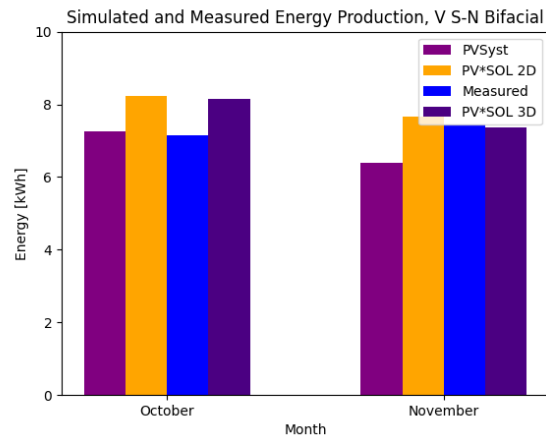
(d) Comparison for the vertical South/North panel

Figure 4.1: Simulated versus measured Energy production for the different configurations.

The following tables display the energy production per configuration per month for the software and how much they deviate from the measured values. The models used for DHI and transposition modelling are still Erbs and Perez, respectively.

Table 4.1: Simulated energy production for a 44°tilted bifacial panel facing South.

	October [kWh]	Deviation [%]	November [kWh]	Deviation [%]
Measured	7.49	-	5.62	-
PVsyst	7.49	0.10	5.65	0.46
PV*SOL 2D	7.75	3.61	6.31	12.2
PV*SOL 3D	7.64	2.21	6.09	8.27

Table 4.2: Simulated energy production for a vertical East/West facing bifacial panel.

	October [kWh]	Deviation [%]	November [kWh]	Deviation [%]
Measured	5.05	-	2.54	-
PVsyst	4.17	-17.4	2.70	6.32
PV*SOL 2D	5.28	4.49	3.63	43.4
PV*SOL 3D	5.18	2.57	3.42	34.7

Table 4.3: Simulated energy production for a vertical South/North bifacial panel.

	October [kWh]	Deviation [%]	November [kWh]	Deviation [%]
Measured	7.13	-	7,45	-
PVsyst	7.28	1.87	6.39	-14.3
PV*SOL 2D	8.23	15.4	7.65	2.62
PV*SOL 3D	8.14	14.11	7.37	-1.08

Table 4.4: Simulated energy production for a bifacial two-axis tracking panel.

	October [kWh]	Deviation [%]	November [kWh]	Deviation [%]
Measured	8.31	-	7.79	-
PV*SOL 2D	8.91	7.21	8.05	3.26

4.2 Annual Simulated Energy Production

Figures 4.4a, 4.4b and 4.4c show the annual production per month per configuration by PV*SOL2D, 3D and in PVsyst, respectively. The meteo data used for this are from Meteonorm 8.1 and are based on 15 years of climate data from Værnes, which is located 35 km North of Trondheim. The annual production predicted for each configuration is shown in Table 4.5.

(a) Simulated annual energy production by PV*SOL 2D

(b) Simulated annual energy production by PV*SOL 3D

(c) Simulated annual energy production by PVsyst
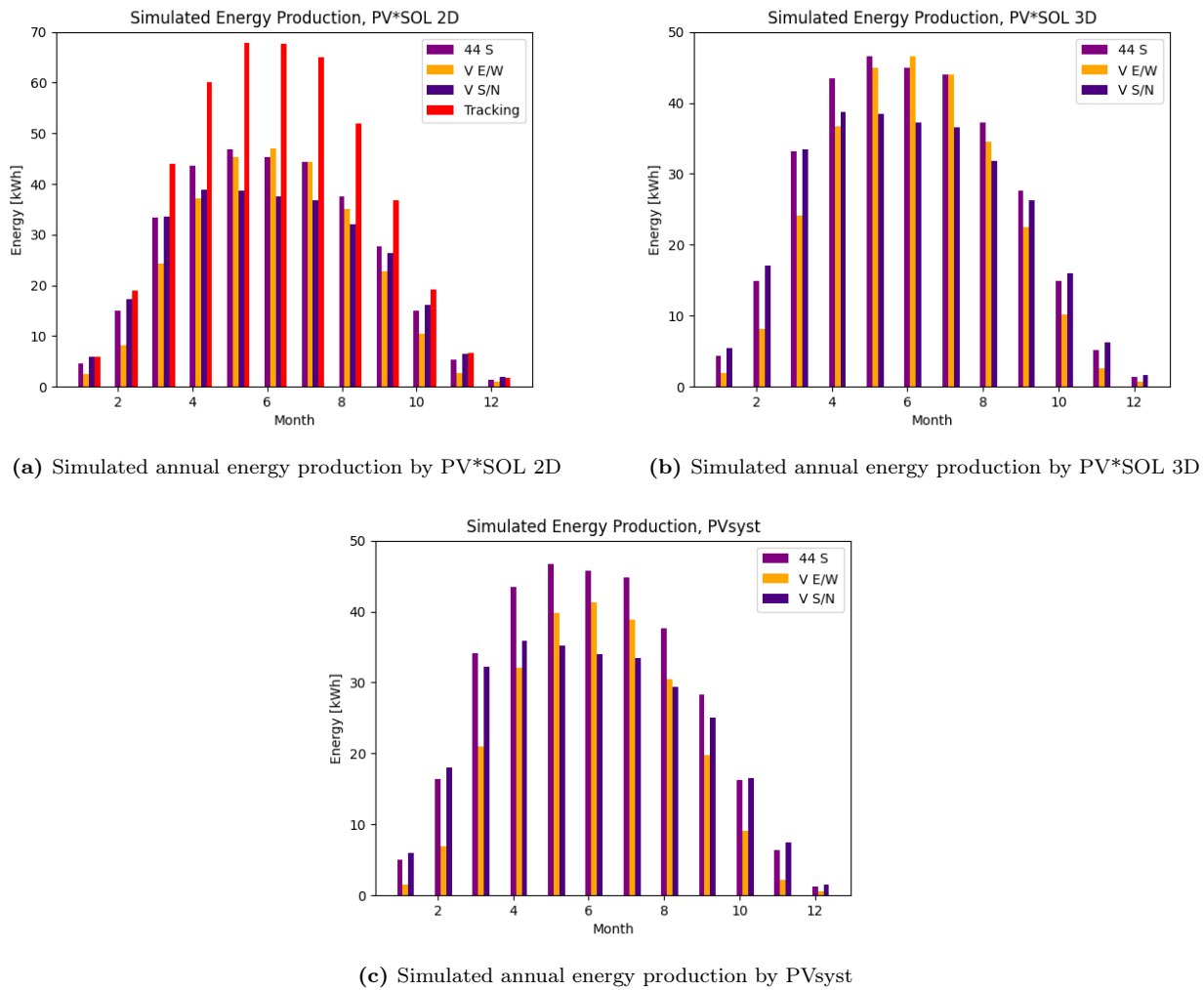
Figure 4.3: Predicted annual energy production by PV*SOL and PVsyst.

Table 4.5: Predicted annual energy production of the different configurations based on meteo data from Meteonorm 8.1.

Software	44°S [kWh]	Vertical E/W [kWh]	Vertical S/N [kWh]	Tracking [kWh]
PV*SOL 2D	320.27	280.54	291.43	445.70
PV*SOL 3D	317.56	276.99	288.78	-
PVsyst	325.98	243.34	274.83	-

4.3   The performance of the diffusive models

This section looks at the performance of the different decomposition models available in PV*SOL. The models in Table 4.6 are displayed in order from the oldest at the top to the newest at the bottom. PVsyst only has one model, which is the Erbs model, which is also an option in PV*SOL. The best performing models are highlighted in bold.

Table 4.6: Relative root mean square deviation, rRMSD, and relative mean bias deviation, rMBD, are displayed in percentage per month for the different DHI models. The lowest deviations are highlighted in bold.

	October		November		December	
DHI model	rRMSD [%]	rMBD [%]	rRMSD [%]	rMBD [%]	rRMSD [%]	rMBD [%]
Orgill	20.02	1.36	35.24	-6.74	42.18	-37.00
Erbs	**19.68**	**-0.46**	35.20	-7.76	42.18	-37.00
Reindl	20.87	4.6	**34.35**	**- 4.61**	42.18	-37.00
Perez	29.05	10.59	52.27	-15.19	42.18	-37.00
Skartveit	20.01	2.86	39.56	-12.07	42.18	-37.00
Boland	21.45	-1.75	37.33	-4.65	42.18	-37.00
Hofmann	23.15	5.42	47.71	-11.39	42.18	-37.00
PVsyst	19.73	-0.81	37.2	0.26	51.54	-7.3

4.3.1   The performance of the diffusive models based on overcast, partly overcast and clear sky

conditions. To get a better picture of the different diffusive models, they are divided into three categories based on the sky conditions; fully overcast, partly overcast, and clear sky.

Fully overcast

The DHI models plotted for three different days with overcast sky conditions are shown in Figure 2.5. The corresponding deviations are presented in Table 4.7, where the lowest deviations are highlighted in bold.
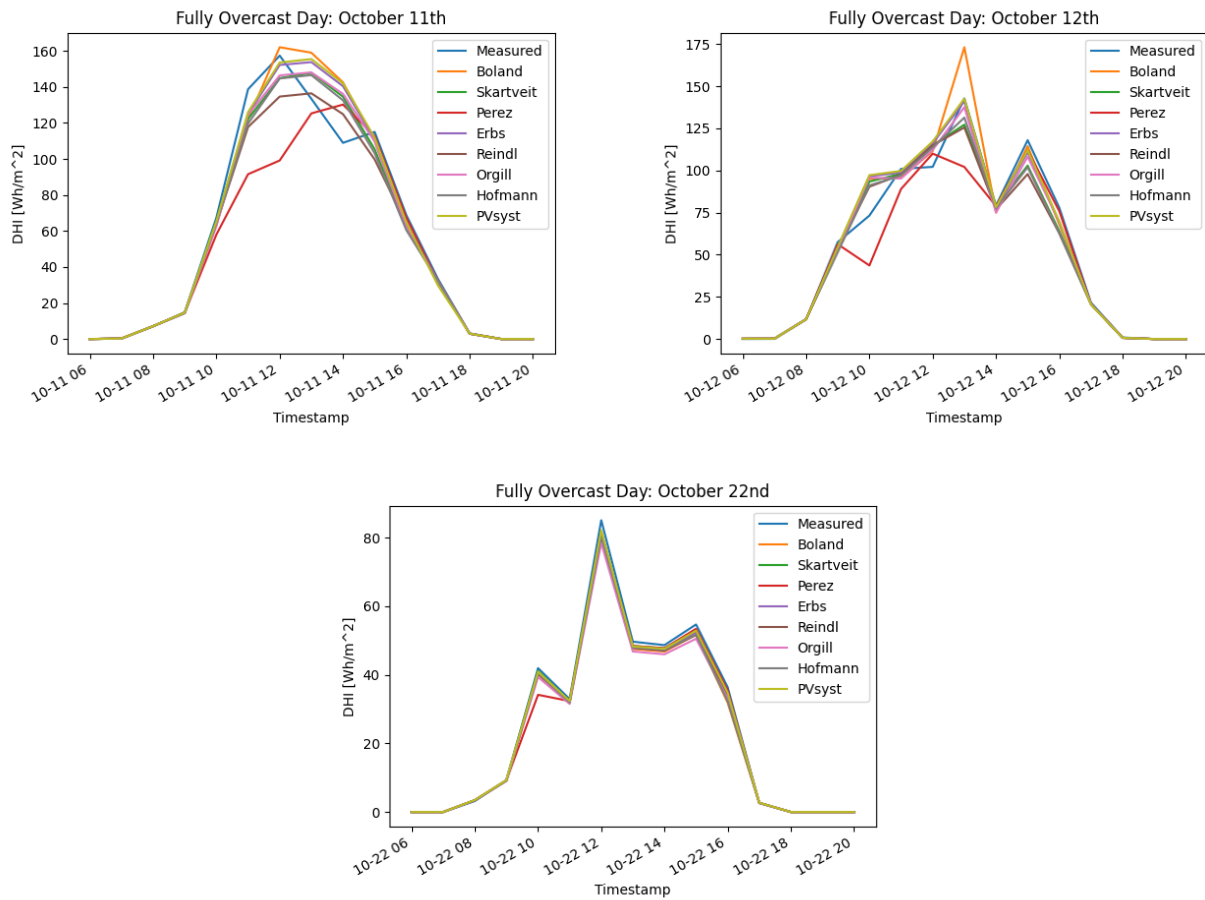
Figure 4.5: DHI plotted for three different overcast sky days.

Table 4.7: rRMSD and rMBD for fully overcast sky days.

Model	rRMSD [%]	rMBD [%]
Orgill	**11.11**	1.59
Erbs	11.36	**-0.88**
Reindl	13.01	4.95
Perez	24.53	10.38
Skartveit	12.09	2.02
Boland	13.54	-2.19
Hofmann	12.05	3.11
PVsyst	11.56	-1.72

Partly overcast

The models were plotted for three different days with partly overcast sky conditions, as seen in Figure 2.7. The corresponding deviations are presented in Table 4.8, where the lowest deviations are highlighted in bold.
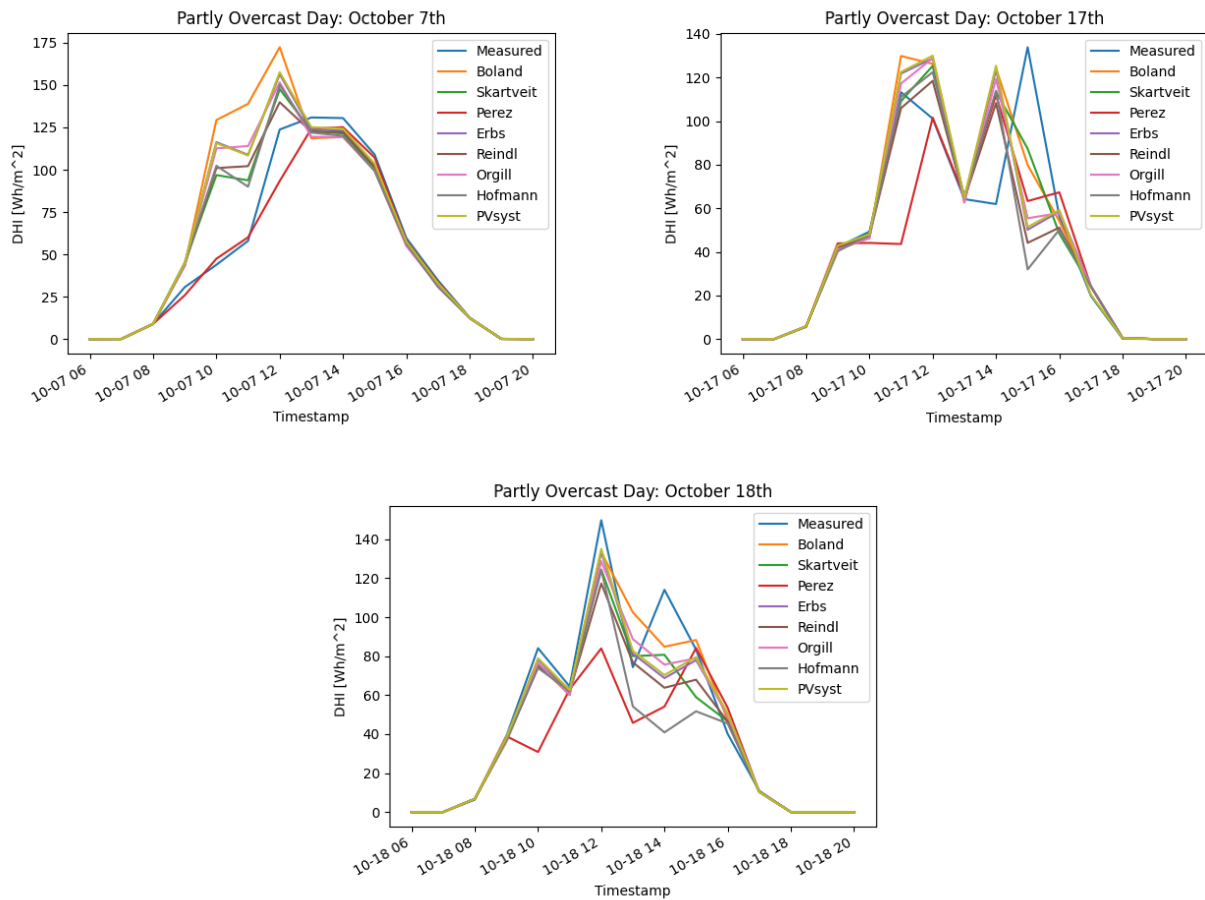
Figure 4.7: DHI plotted for three different days with a partly overcast sky.

Table 4.8: rRMSD and rMBD for the different DHI models for partly overcast sky days.

Model	rRMSD [%]	rMBD [%]
Orgill	32.8	-3,99
Erbs	33.59	-5.09
Reindl	33.84	1.87
Perez	43.6	15.42
Skartveit	**26.19**	**-1.75**
Boland	33.85	-10.43
Hofmann	39.18	4.93
PVsyst	33.17	-5.9

Clear sky

The models were plotted for three different days with clear sky conditions, as seen in Figure 4.9. The corresponding deviations are presented in Table 4.9, where the lowest deviations are highlighted in bold.
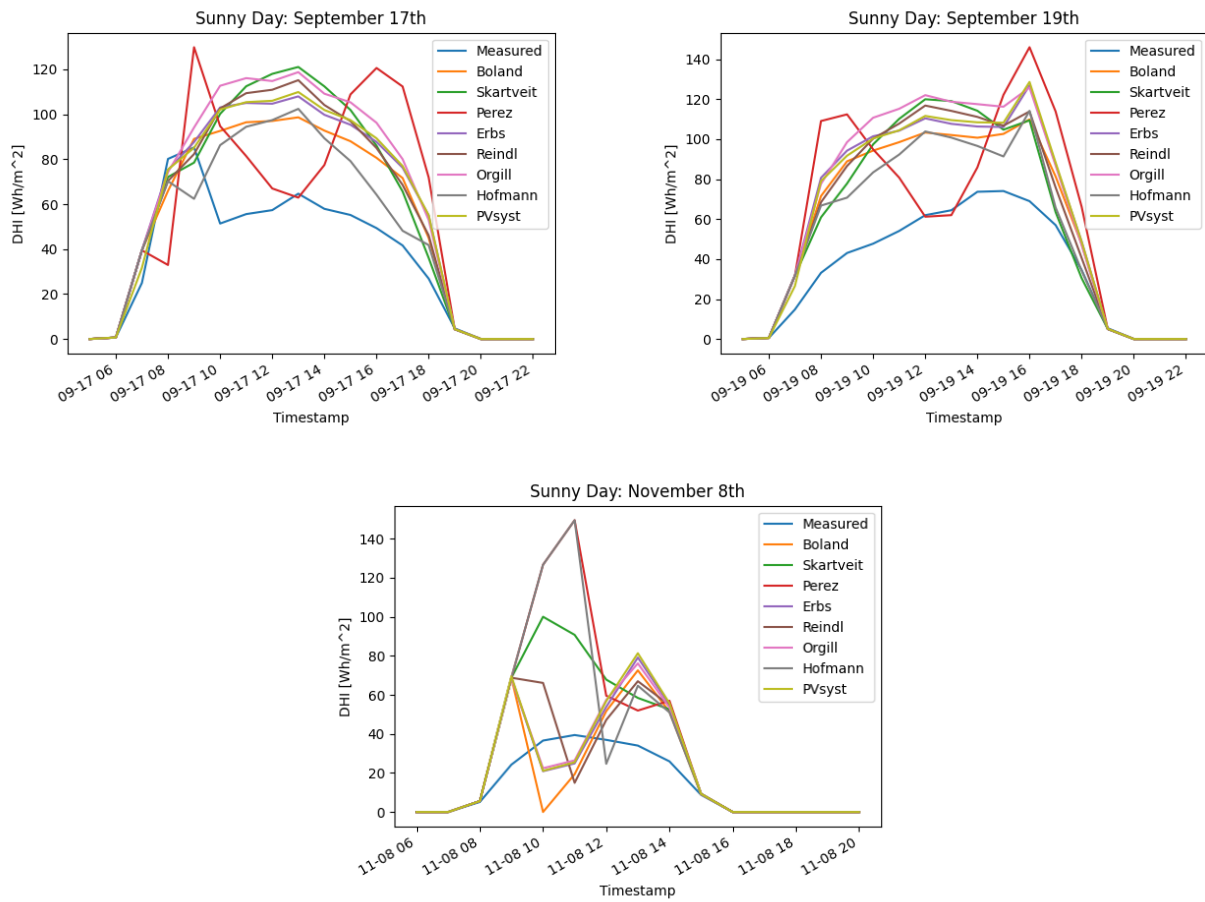
Figure 4.9: DHI was plotted for three different clear-sky days.

Table 4.9: rRMSD and rMBD for the different DHI models for clear sky days.

Model	rRMSD [%]	rMBD [%]
Orgill	47.19	-74.08
Erbs	44.06	-64.71
Reindl	43.86	-63.24
Perez	53.34	-74.93
Skartveit	45.73	-69.77
Boland	**40.95**	**-51.87**
Hofmann	46.3	-55.81
PVsyst	44.38	-65.13

37

4.4 Performance of the different transposition models of PV*Sol

The rRMSD and rMBD are presented in matrices for each configuration and each software. for each month. In Tables 4.10 and 4.11, rMBD and rRMSD are shown for the 44 S configuration for October. The rest of the tables can be found for each configuration per month in Appendix B and C. The best combination of decomposition and transposition is highlighted in light green, while the best combination overall for each configuration is highlighted in dark green.

Table 4.10: S 44 3D October rMBD

Transposition / DHI model	Liu & Jordan	Hay & Davies	Klucher	Perez	Reindl
Orgill & Hollands	7.51	-0.61	1.36	-6.5	-1.22
Erbs, Klein & Duffe	-0.87	-8.56	-6.97	-15.07	-9.09
Reindl	13.19	5.6	6.84	-1.33	4.86
Perez & Inceichen	5.6	-2.76	-1.08	-8.17	-3.45
Skartveit	4.32	-7.49	-1.96	-9.16	-4.11
Boland, Ridley & Laurent	11.83	4.5	6.06	-2.11	3.84
Hoffman	9.61	1.65	2.95	-5.12	0.9

Table 4.11: S 44 3D October rRMSD

Transposition / DHI model	Liu & Jordan	Hay & Davies	Klucher	Perez	Reindl
Orgill & Hollands	31.66	29.94	28.4	28.38	29.87
Erbs, Klein & Duffe	29.91	31.14	29.85	30.88	31.21
Reindl	38.98	32.81	32.36	29.67	32.48
Perez & Inceichen	32.97	30.97	29.84	30.35	30.9
Skartveit	34.32	32.8	31.32	31.2	32.32
Boland, Ridley & Laurent	36.53	32.48	31.65	29.99	32.25
Hoffman	35.59	31.64	30.77	29.52	31.44

4.4.1 Best performing model combinations

Based on all the matrices in Appendix B and C, Table 4.12 displays some of the best performing models per configuration. For visualisation of the models, see the figures following the table. All of these results are based on 3D modelling, except for the tracking, which is based on 2D modelling.

Table 4.12: rRMSD and rMBD of the best performing models for each configuration for October and November. The lowest deviations per model are highlighted in bold.

		October		November	
Configuration	Model combination	rRMSD [%]	rMBD [%]	rRMSD [%]	rMBD [%]
44 S	Orgill + Hay	**29.94**	**-0.61**	**42.4**	8.58
	Perez + Hay	30.97	-2.76	46.95	**-1.22**
	Erbs + Perez	30.88	-15.1	47.86	-8.24
V E/W	Erbs + Liu	65.03	**1.78**	89.32	19.78
	Reindl + Liu	73.95	3.7	52.14	**-7.08**
	Erbs + Perez	**56.92**	-15.07	**42.13**	-26.17
V S/N	Orgill + Liu	**32.7**	**-2.38**	60.62	30.88
	Skartveit + Perez	35.61	-23.41	**35.43**	**-0.6**
	Erbs + Perez	37.3	-30.97	41.29	0.96
Tracking	Boland + Reindl	40.94	**0.02**	48.8	12.49
	Perez & Hay	42.7	-9.14	46.29	5.70
	Erbs+ Perez	**37.86**	-24.9	**40.11**	**0.07**

44°tilt towards South

Figure 4.10 shows the monthly measured data for the 44S configuration compared to the best performing models. Figure 4.11 shows a daily comparison of two of the comparing models in October.
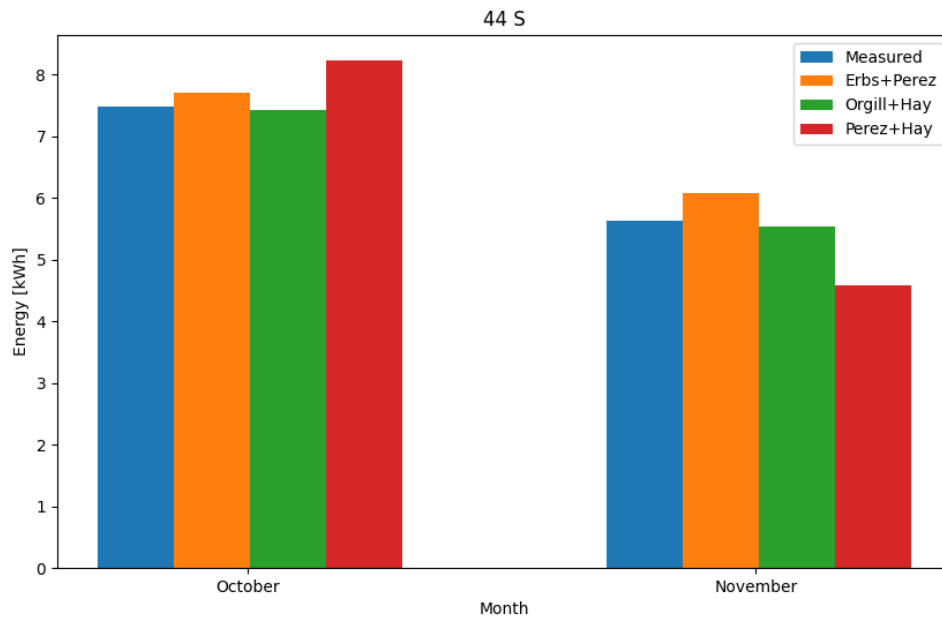
Figure 4.10: Comparison of the best model for the 44 S configuration
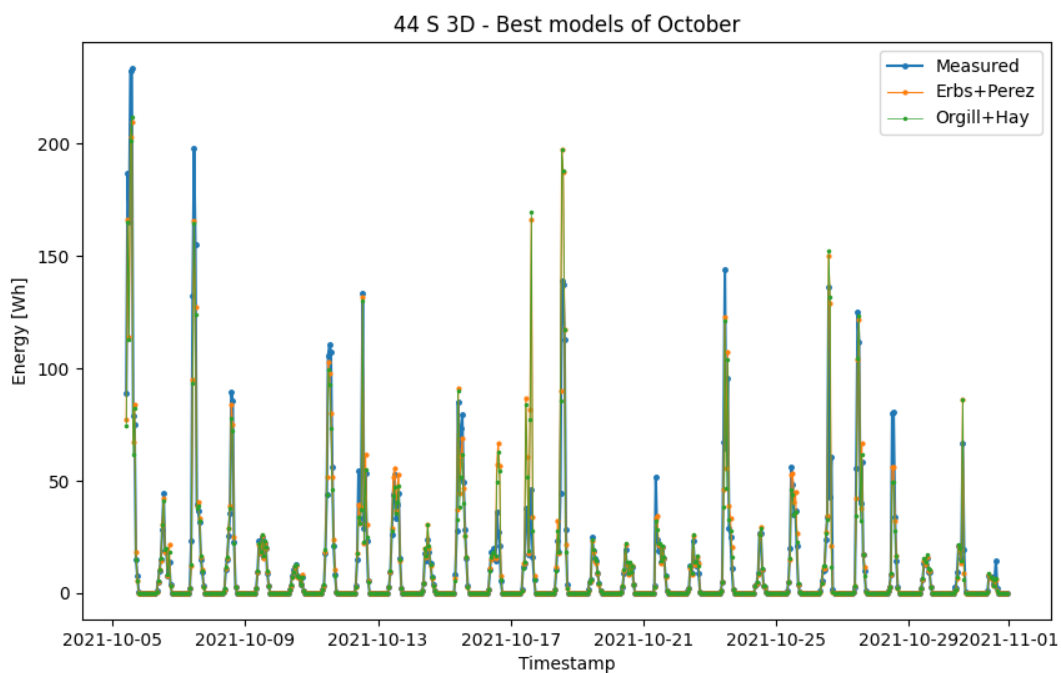
Figure 4.11: The best model compared to Erbs+Perez and measured values for the 44 S configuration for October.

Vertical East/West

Figure 4.12 shows the monthly measured data for the V E/W configuration compared to the best performing models. Figure 4.13 shows a daily comparison of two of the competing models in October.
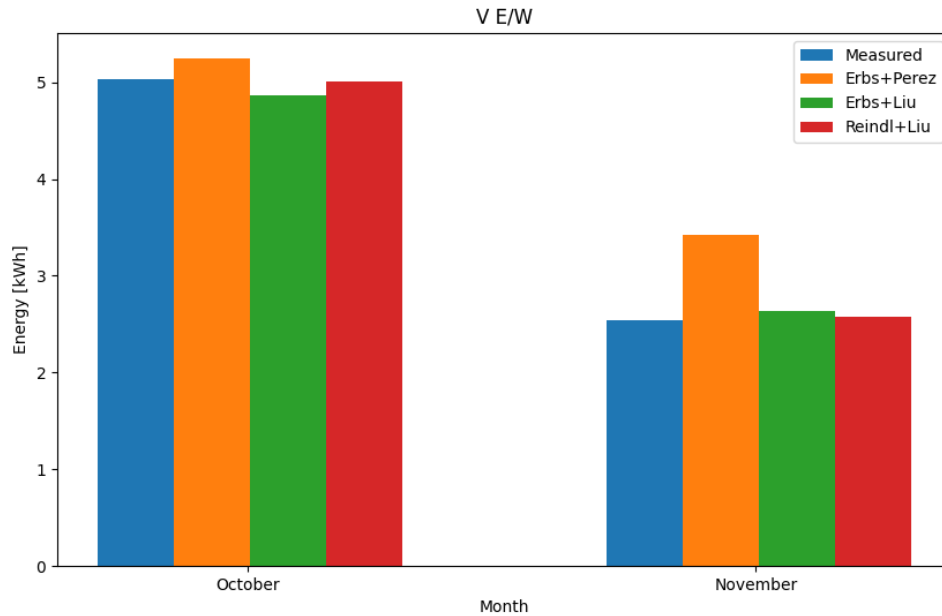
Figure 4.12: Comparison of the best model for the V E/W configuration
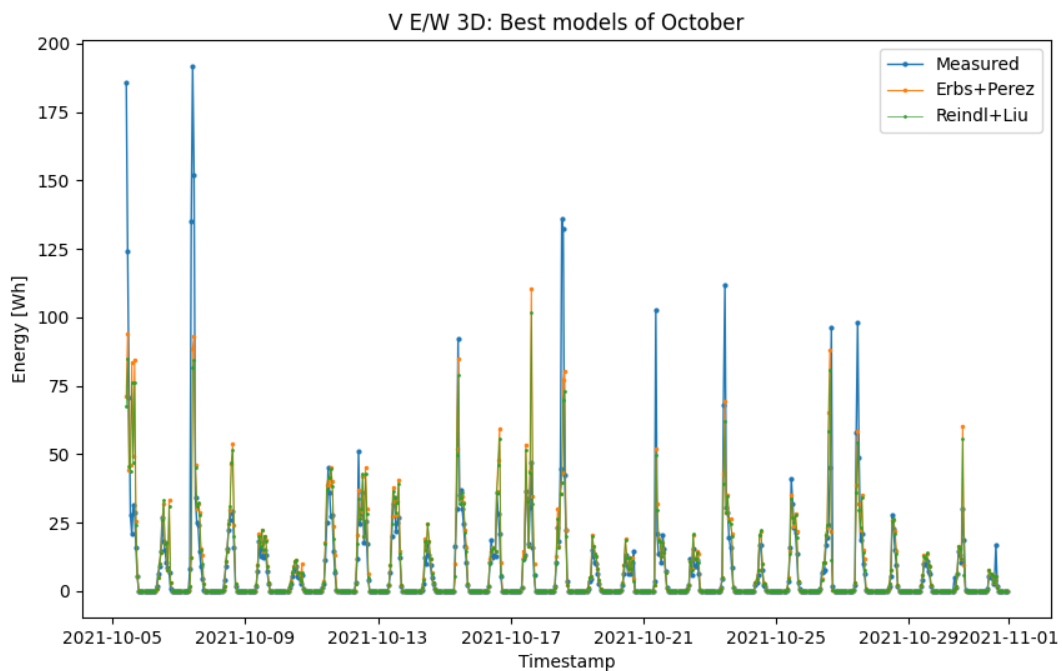
Figure 4.13: The best model compared to Erbs+Perez and measured values for the V E/W configuration for October.

Vertical South/North

Figure 4.14 shows the monthly measured data for the V S/N configuration compared to the best performing models. Figure 4.15 shows a daily comparison of two of the competing models in October.
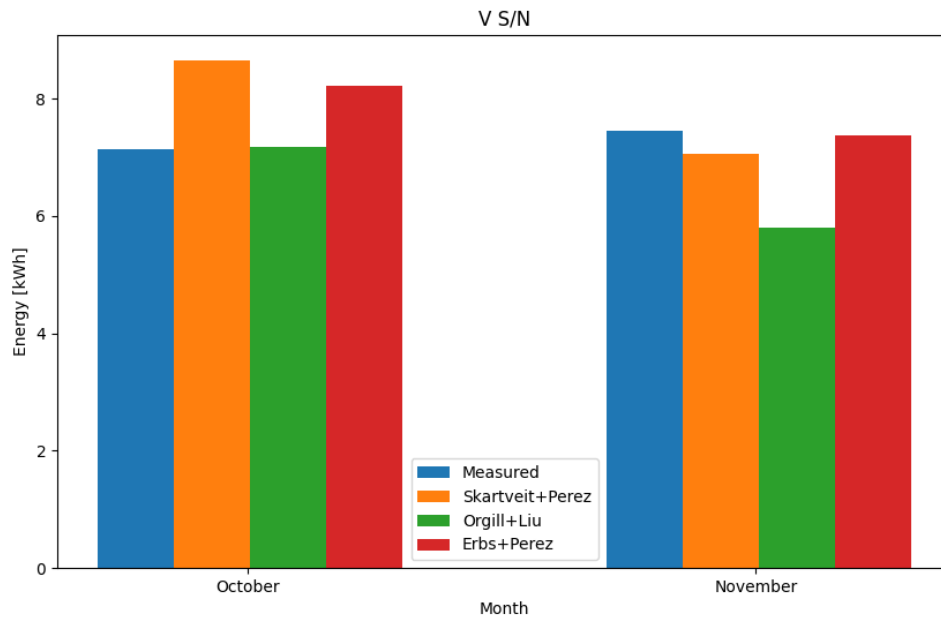
Figure 4.14: Comparison of the best model for the V S/N configuration
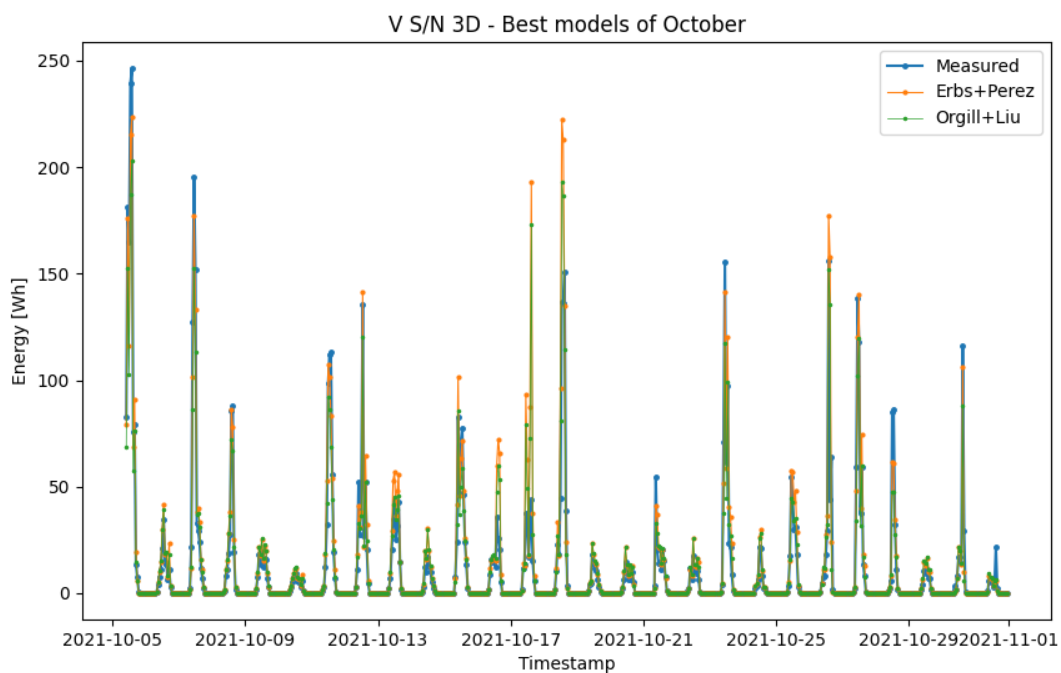
Figure 4.15: The best model compared to Erbs+Perez and measured values for the V S/N configuration for October.

Two-axis tracking

Figure 4.17 shows the monthly measured data for the two-axis tracking configuration compared to the best performing models. Figure 4.16 shows a daily comparison of two of the models competing in October.
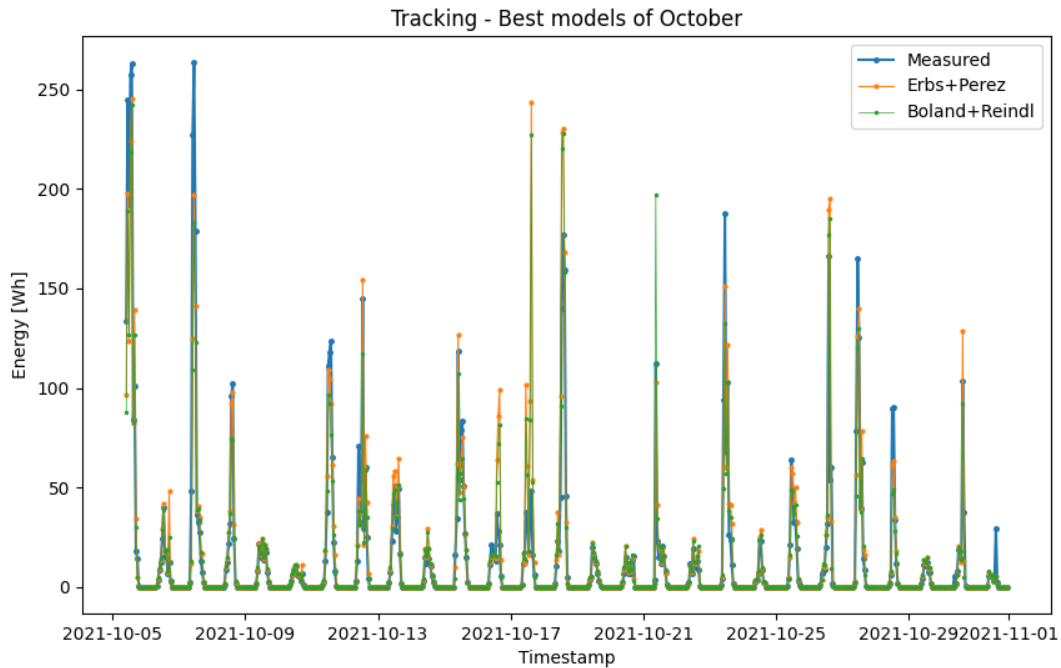
Figure 4.16: The best model compared to Erbs+Perez and measured values for the two-axis tracking for October.
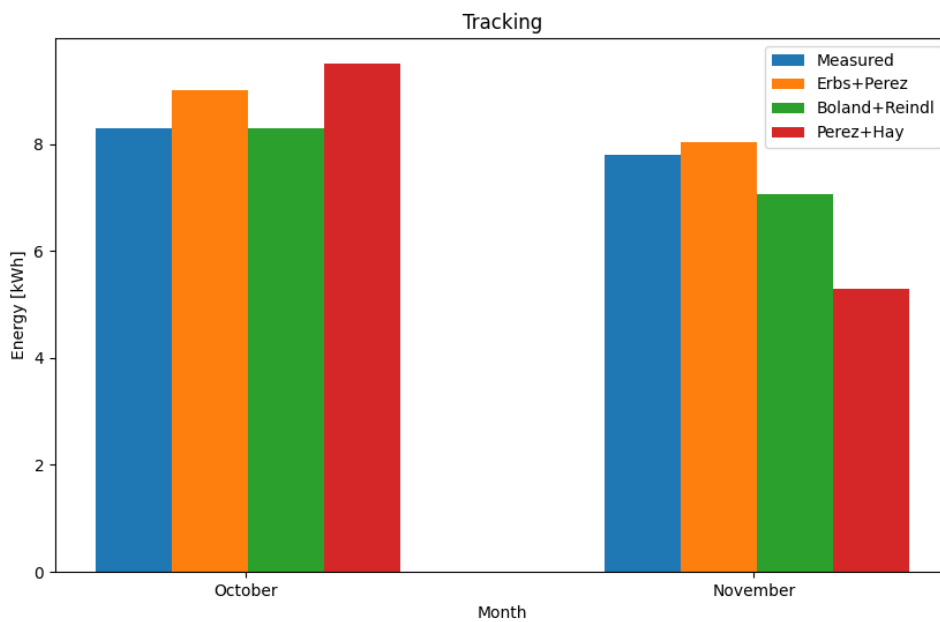
Figure 4.17: Comparison of the best model for the two-axis tracking.

4.5   Performance of the different transposition models of PVsyst

The tables below show the rRMSE and rMBE for the different configurations for October and November and for the two combined months. The tables on the left show the results based on Perez's transposition model, whereas the tables on the right show the results based on Hay's transposition model.

Table 4.13: Deviations for Perez and Hay for the 44 S configuration

Perez	Oct	Nov	Oct+Nov
rRMSE [%]	29.66	50.46	41.89
rMBE [%]	-0.9	-1.96	-1.36

Hay	Oct	Nov	Oct+Nov
rRMSE	31.77	51.15	43.57
rMBE	3.52	-3.32	0.58

Table 4.14: Deviations for Perez and Hay for the V E/W configuration

Perez	Oct	Nov	Oct+Nov
rRMSE	79.11	48.02	63.01
rMBE	20.97	-13.23	9.52

Hay	Oct	Nov	Oct+Nov
rRMSE	80.8	48.93	63.37
rMBE	18	-16.74	6.37

Table 4.15: Deviations for Perez and Hay for the V S/N configuration

Perez	Oct	Nov	Oct+Nov
rRMSE	33.34	42.3	38.87
rMBE	-2.99	12.5	4.93

Hay	Oct	Nov	Oct+Nov
rRMSE	35.77	44.01	41.06
rMBE	2.55	12.66	7.72

The following figures show the two options of transposition models available in PVsyst for each day of October. Figure 4.18 shows the 44S configuration, while Figures 4.19 and 4.20 show the vertical E/W and the vertical S/N configurations, respectively.
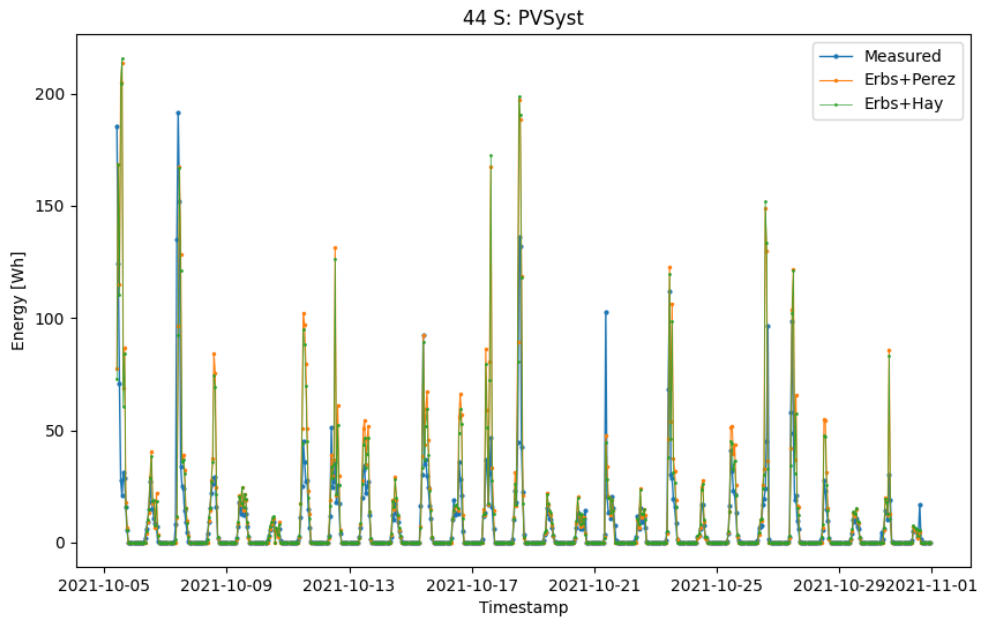
Figure 4.18: The two transposition models of PVsyst compared to measured values for the 44 S configuration for October.
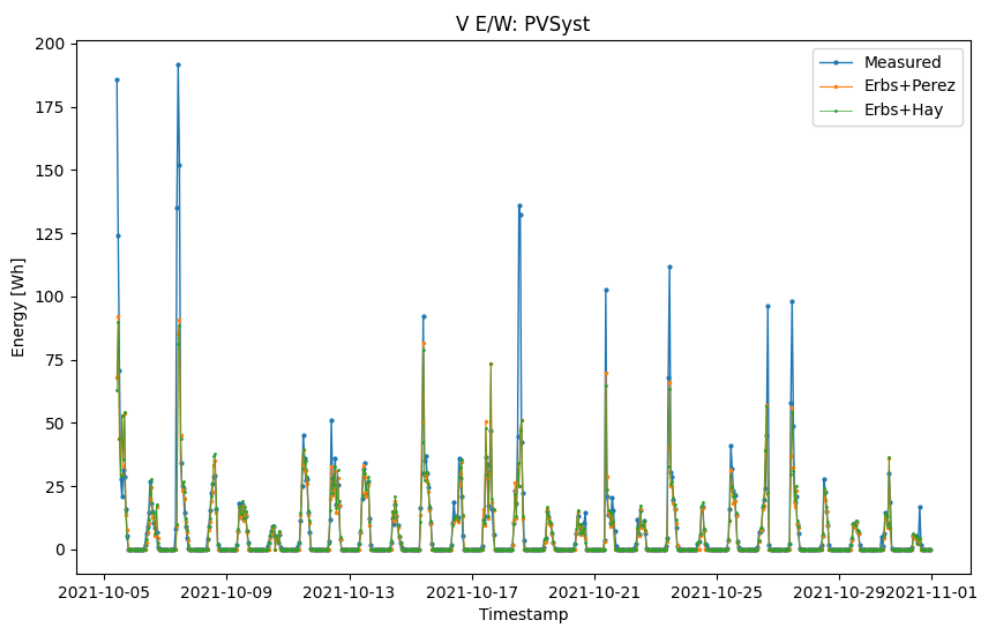
Figure 4.19: The two transposition models of PVsyst compared to measured values for the V E/W configuration for October.
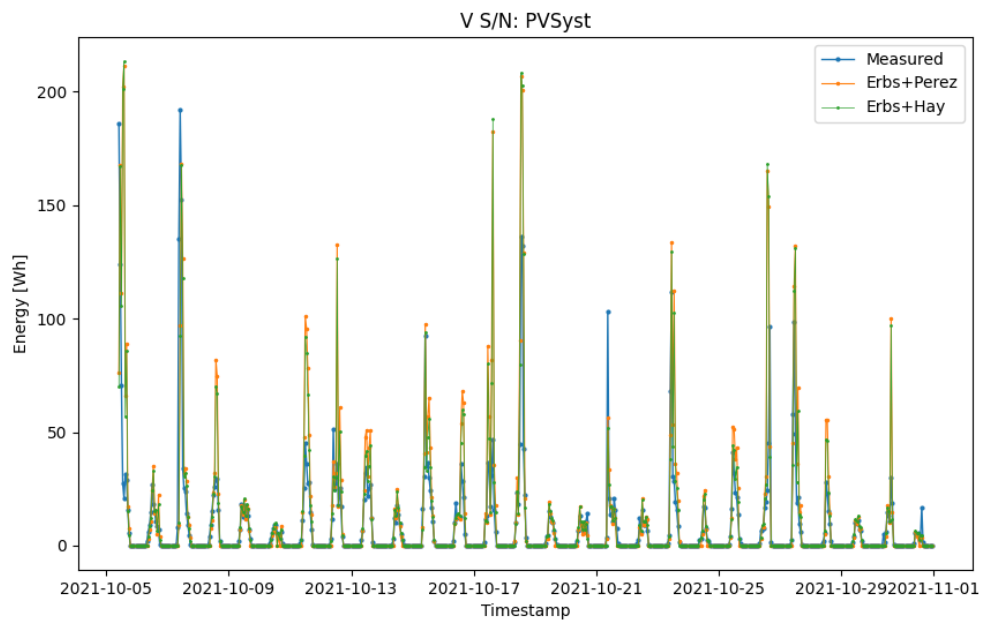
Figure 4.20: The two transposition models of PVsyst compared to measured values for the V S/N configuration for October.

5 Discussion

This section explores the significance of all the results presented in the previous section in the same order as they are presented. The results are critically assessed as well as the limitations of the research.

5.1 Simulated versus Measured Energy Production

The results in Section 4.1, show that for a fixed 44°tilt toward South, both PVSyst and PV*SOL predict a reasonably energy production compared to the measured values. The 2D simulation from PV*SOL is deviating a lot for November, however, the 3D simulation is slightly better keeping within a 10% deviation. PVsyst is simulating close to the measured values keeping within 1% for both months. Note that PVsyst is only based on 2D modelling, but still performs better than both the 2D and the 3D modelling of PV*SOL for the S44 panel. The two software handle the bifacial modelling differently, which could be the reason for the deviation, even though the models used are the same and the inputs are the same or very similar as explained in Section 3.

Based on the two months of modelling, neither PV*SOL nor PVsyst show good results for the vertical bifacial systems. The deviation is not consistent for the two months. For the E/W configuration, PVsyst greatly underestimates the production in October and slightly overestimates in November, while PV*SOL slightly overestimates in October and significantly overestimates in November by 34%. As explained in Section 2.7.1, the way PV*SOL handles radiation in the plane is different with vertical configurations than with an inclined plane. In addition, it is harder to predict how much irradiance will hit the rear side, which is highly dependent on albedo and surrounding objects, as explained in Section 2.2.4.

The South/North configuration suffers from the same issue, the deviation is not consistent over the two months. However, the deviation is slightly smaller for the South/North configuration. Since this vertical configuration shows slightly better results than the E/W configuration, the results indicate that the software better transposes the irradiance to south-facing configurations. The higher deviations for the vertical panels are consistent with the literature, as mentioned in Section 2.6.

The two-axis tracking is within a reasonable deviation below 10% for both months. This makes sense since it follows the Sun throughout the day, thus the irradiance hitting the plane will be the DNI modelled from the decomposition models. The reflected and diffuse light hitting the front side and rear side is more complex to model on the other hand. This indicates that the software struggles to compute how much direct light a panel is absorbing when the panels are in the vertical configurations, and how much of the diffuse and reflected light is absorbed.

These results are only based on one panel, which means that the self-shading effects called

attention to in Section 2.2.4 are small, and the parameters affecting the bifacial gain from Section 2.2.1 like the ground coverage ratio and row-to-row distance, are not considered. The results of a roof covered with panels would be different. For example, for vertical panels, the row-to-row distance would be larger to reduce the amount of self-shading, compared to rows of tilted panels. However, vertical panels open up for different and more creative uses, such as in agrivoltaics, or they could serve as a railing for rooftops, leaving the roof space available for other purposes.

5.2 Optimal configuration based on simulated data

Based on the results of Section 4.2, the best fixed configuration in both PV*SOL and PVsyst is S44. Of course, the tracking system shows the highest energy production, more than 100 kWh a year than S44, based on the simulation. PV*SOL estimates the vertical east / west configuration to be the best in June, while PVsyst suggests that S44 is the best throughout all the summer months. Overall, the vertical South/North configuration produces more energy than the East/West configuration for both software. 11% more for PVsyst and 4% for PV*SOL, both 2D and 3D, over a year. 4% is of the same magnitude as the results of Mubarak et al. described in Section 2.2.5. In that case, the East/West configuration is economically beneficial in case of high electricity prices, which have been an increasing issue in Norway over the past year. Furthermore, V E/W would be good in the summer to obtain a wider range of energy production, which is profitable for industries or households not using too much energy in the middle of the day. However, the South/North configuration produces more energy, so if most of the energy consumption is in the middle of the day, the vertical S/N would be more profitable, if one had to choose between the two. If the difference is 11%, the economic profit may not compensate for the loss in energy production. This would require more research, and the results should be compared to measured data to get an accurate picture of the reality. In addition, as discussed in the previous section, the simulations of the vertical panels deviate a lot from the measured results. This will also affect the results in this section and will not give a precise picture of the production of vertical installations.

If the entire roof were to be covered with bifacial panels, the 44°tilt toward the South would be the preferred configuration based on these results, since it is the fixed configuration with the highest energy production. This configuration would also require a smaller area than the vertical panels in terms of row-to-row distance. However, urbanisation has made rooftops a social area, and covering the roof with solar panels is not always an option. On top of apartment buildings, the roof is often a terrace or green space, making the space unavailable for solar panels. Using the vertical bifacial panels as a railing around the roof could be an option in these cases, or using them in a synergistic way with the green spaces like in agrivoltaics. It would be interesting to investigate further how much one would lose in terms of energy production on this versus covering the roof with the S44 configuration.

A weakness of this analysis is the fact that the results are based on meteo data from 1991 to 2006. The climate has changed a lot during the last two decades, so the results may not be applicable today. A whole year of measured results is needed to investigate this matter further and verify the modelling by the software.

5.3   DHI models

Table 4.6, shows the same value for all the models available in PV*SOL in December. Valentine Software, the owner of the software, was contacted multiple times regarding this issue, without getting any response. When checking lower latitudes in Europe, this is not an issue, so it seems like a high-latitude problem. In the winter, the Sun barely reaches above the horizon, so PV*SOL estimates almost all of the GHI to be diffuse for December. Here, some non-adjustable settings in the software must be the issue, since the only user input is the meteo file, horizon, and type of decomposition model, which affects the DHI. PVsyst has only one model, so it is not possible to know if this is also the case with this software. It does show a way lower rMBD, so at least it models closer to the measured value, however, the rRMSD is higher. The results indicate that the software cannot cover high latitudes in December. For the rest of the analysis, December will be disregarded due to this limitation in the software.

The monthly results in Table 4.6 show that the Erbs model has the best accuracy in October and Reindl the best in November for PV*SOL. PVsyst is also based on the Erbs model, which is quite close to the Erbs model in PV*SOL in October, but deviates quite a bit in November with around 7%. Again, the user input is completely the same in both software, which indicates that something in the software, unidentifiable to the user, is different between the two.

Orgill, Erbs, Reindl, and Boland all show reasonably low deviations based on the results of the two months, while Perez sticks out with over 10% deviation for both months. Both Skartveit and Hofmann also show high deviations in November. Skartveit is developed and tuned to data from Bergen, Norway, which one might have thought had benefited the model, but the results show otherwise. As explained in Section 2.2.3, Norway has a diverse climate depending on location. Bergen is a coastal city with a lot of rain further South in Norway than Trondheim, and it could be why Skartveit performs poorly in November, as it had more clear weather than in October.

On the basis of the overcast days, the deviations in DHI are small compared to the other sky conditions. Erbs shows the overall best results for overcast days. This is probably why Erbs is also the best model in October because October was an unusually cloudy month. Again, Perez shows poor performance both with respect to rRMSD and rMBD. On the day with the lowest irradiance, 22 October, all models fit the curve well, which is consistent with the literature in Section 2.5. The results show that the more overcast the weather, the better the decomposition models perform, which is not consistent with the literature. According to the

literature, partly overcast sky conditions should be the hardest to model and therefore have the highest deviations. The reason why this is not the case here might be that the days that are chosen lean more towards the overcast sky conditions, rather than clear sky conditions.

Based on the results from a partly overcast sky, Skartveit is the best performing model, while Perez still shows bad performance. Hofmann has a high rRMSD, but an okay rMBD, while Boland shows a higher rMBD but a lower rRMSD. The other models show relatively low deviations. Perez claims that the model is especially appropriate for intermediate sky conditions, yet all the other models show a better performance. However, in Figure 4.7, on October 17, the Perez model simulates the closest to the measured values, but this is not the case for the other two days.

For clear-sky days, Boland shows the best results. This model was developed in Australia with clear sky weather, which could be the reason for the good behaviour. Again, Perez shows the poorest performance with respect to both rRMSD and rMBD. In general, all models overestimate the diffuse radiation for all of these days. Figure 4.9 shows that on both September 17th and 19th, Perez has a different trend from all the other models, while on November 8th it is not far from the other models. The simulation was run several times to check for any errors made during the simulations, but none were found. Perez was the first model to differ from the ones that were based on Liu's model, which might be why it is so inaccurate. As mentioned in Section 2.5, the article by Gueymard et al. showed inconsistent results for this model, so the results are in line with the literature.

Based on the results from the DHI modelling, the Perez decomposition model is not fit for modelling DHI at high latitudes like Trondheim, while Orgill, Erbs, Reindl, and Boland show lower deviations, and are appropriate models to use.

5.4 Transposition models

For the analysis of the transposition models, the energy was evaluated instead of the irradiance in the plane of the module because such measured values were not available. This means that the given values may contain some errors due to other simulation parameters in the software, but since the goal of the thesis is to find the best model combination for the different configurations in Trondheim, this analysis is sufficient for that purpose.

Based on the matrices shown in Section 4.4, it is clear that rMBD and rRMSD do not favour the same model. To find the best model, both were minimised. Looking at Figure 4.10, the model combination; Erbs + Perez shows accurate results, but Orgill + Hay shows the closest result based on the monthly energy production. Based on the hourly values shown in Figure 4.11, both models are close to each other. When choosing between the two models, the choice will not have a significant influence on the results for this configuration. The combination of Perez + Hay shows a low rMBD, but the results in Figure 4.10 show poor performance.

This agrees with the results of Section 4.3, where Perez showed the poorest performance of the decomposition models. The low deviation by Hay&Davies is confirmed by the literature in Section 2.6.

For the V E/W configuration, both combinations Erbs + Liu and Reindl + Liu show a good energy estimation in Figure 4.12. However, when looking at Figure 4.13, the models do not fit the measured values as well for the other configurations. This can also be seen in their respective rRMSD values. This supports the discussion in Section 5.1, about the modelling of the vertical configurations not being very accurate. However, when changing from the Erbs + Perez model to the Erbs + Liu model, the monthly results improved a lot. So, even though the model does not fit too closely on an hourly or daily basis, the purpose of the software is to predict the energy production over a larger time period, like months or years. For this purpose, the Erbs + Liu combination shows promising results for this configuration.

For the vertical S/N configuration, the Orgill + Liu combination is very close for October, but in November the Erbs + Perez combination shows the closest results according to Figure 4.14. Looking at Figure 4.15, Erbs + Perez overestimates the production on days with high radiation, more than Orgill + Liu. This indicates that Orgill + Liu performs better in the months with a lot of overcast weather. October, only had one day with clear-sky conditions, which was October 5th. Here, the Erbs + Perez combination is closer than Orgill + Liu. Erbs + Perez is the best model for November for V S/N, which had more clear weather than October, so, based on the results, this model combination is more suitable for clearer weather for this configuration.

Based on Figure 4.17, Boland + Reindl show a good performance for October, while Erbs + Perez is the best in November. This supports the earlier discussion about the Erbs + Perez combination being better for clearer weather conditions. Perez + Hay show large deviations even though the rRMSD and rMBD are fairly low. These results are not consistent over the two months, overestimating in October and underestimating in November. Both Erbs + Perez and Boland + Reindl show low deviations and are good to use based on these two analysed months.

PVsyst only has one decomposition model, and two transposition models, Perez and Hay. The two transposition models do not deviate much from each other, but Perez is slightly more accurate. For the vertical configurations, the Hay shows a closer rMBD, while the rRMSD is slightly higher. The two are still so close that either model can be used. For the E/W configuration, it can be seen in Figure 4.19 that the models struggle to simulate the higher energy production peaks, while the 44 S and the V S/N show a more similar performance. This is similar to the behaviour of the models in PV*SOL, too.

5.5 Comparison of the software

PV*SOL and PVsyst are widely used in the PV industry. PV*SOL is more expensive than PVsyst but in return is more user friendly. The user interface is more intuitive than that of PVsyst, and educational videos and information on how to work the software are easier accessible for PV*SOL. Especially for 3D simulation, PV*SOL has a more user-friendly interface. The 3D simulation in PVsyst was attempted to use, but the software kept crashing. Therefore and due to time limitations, only the 2D simulation in PVsyst was used. When it comes to the bifacial modelling, PV*SOL is also more intuitive than PVsyst. Choosing "unlimited shed" in PVsyst when modelling bifacial PV, is not the most obvious option. PV*SOL is also the software that can model a bifacial two-axis tracking system in 2D. This feature is still missing in 3D and PVsyst can only model one-axis tracking.

When looking at the modelling, PVsyst hits closer to the measured values than PV*SOL for the S44 configuration when choosing the Erbs + Perez combination. When changing the models for PV*SOL however, PV*SOL is competing. For December however, PV*SOL show poor behaviour, if this is the case for PVsyst as well cannot be found out, since it only has one decomposition model.

6 Conclusion

In this Master thesis, data from a new rooftop bifacial PV lab in Trondheim have been investigated. The laboratory has been simulated with two widely used commercial PV software, PV*SOL and PVsyst. Due to restrictions, the available data was only for October and November 2021, which is a too short period of measured data to state any solid and robust conclusions of this work. However, it can provide an overview of the state of the art and point to the direction of the further research needed.

Based on the simulation results, the 44°tilt towards the South is the best configuration for bifacial panels on rooftops in Trondheim, when looking at total energy production. The two-axis tracking produces 100 kWh more a year, but the cost of such a system usually overgoes this extra gain. Depending on the consumer of the energy and the area in which the panels are to be placed, the two vertical configurations compete. A combination of vertical South/North and vertical East/West panels would most likely be a good combination. More research is needed to evaluate this, and preferably research on larger systems where shading effects in a row are taken into account.

For the decomposition models of PV*SOL, the model that stands out is Perez, which shows very high deviations. This model should be avoided when modelling PV systems in Trondheim. The best models are Erbs, Reindl, Boland, and Orgill.

For the combination of decomposition and transposition models, Orgill + Hay showed the best performance for the S44 configuration, and Erbs + Perez is also a good choice. For V E/W Reindl + Liu showed the lowest deviations, and for V S/N Orgill + Liu was best in October, while Skartveit + Perez was best in November. Overall, Erbs + Perez was the closest for this configuration. For the two-axis tracking, Erbs + Perez showed the overall best results. For PVsyst Erbs + Perez shows the best results for all configurations.

Both software simulate vertical configurations poorly when compared based on the same models. Especially, the vertical East/West configuration is simulated poorly in both software. However, when choosing the optimum models in PV*SOL, the deviation decreased. PV*SOL has some problems with the decomposition models in December and is therefore not preferred to use for this month in Trondheim.

On the basis of user experience, PV*SOL has a better user interface but is more expensive than PVsyst. PVsyst also shows slightly lower deviations on the S44 configuration. For the two-axis tracking system, PV*SOL was the only software that offered this type of modelling for bifacial panels.

7   Further work

A recurring limitation in this thesis is the lack of measured data, which is also a problem in the literature. All the analysis done for only two months, which this thesis is based on, should be done for a whole year, which exceeds the time of a master's thesis. The combination of decomposition and transposition models that perform best in October and November might not be the same during the summer, since the climate between seasons differs greatly in the Nordics. In addition, the analysis of the models should preferably be done manually outside the software, to have greater control over all the parameters. When using software, it becomes a black box where the parameters cannot be controlled manually.

The annual simulated energy production of the different configurations needs validation, and the economy on the vertical East/West versus the South/North configuration would be interesting to investigate with regards to electricity prices.

Furthermore, the bifacial gain of the PV system should be quantified, and the simulated bifacial gain of the software should be verified and evaluated.

Lastly, an interesting case would be to simulate the energy production of a whole roof consisting of only bifacial panels of the different configurations and compare these results. For example, vertical panels would need a larger row-to-row distance, but in return, they might produce more than the 44°tilt.

References

[1] H. Birkelund, F. Arnesen, J. Hole, D. Spilde, S. Jelsness, F. Aulie, and I. Haukeli, "Langsiktig kraftmarkedsanalyse 2021-2040," *NVE Rapport*, vol. 29, 10 2021.

[2] "Vector sun orientation." `https://www.pngkey.com/maxpic/u2w7a9q8r5i1w7t4/`. Last accessed 14.11.2021

[3] C. W. Thurston, "Nrel builds first solar database for bifacial albedo." `https://cleantechnica.com/2019/02/18/nrel-builds-first-solar-database-for-bifacial-albedo/`, 2019. Last accessed 09.12.2021

[4] S. B. O. Sunde, "Investigation of different pv systems situated at campus gløshaugen of ntnu in trondheim, norway," 12 2021.

[5] Masson-Delmotte, V. P. Zhai, A. Pirani, S. L. Connors, C. Péan, S. Berger, N. Caud, Y. Chen, L. Goldfarb, M. I. Gomis, M. Huang, K. Leitzell, E. Lonnoy, J. Matthews, T. K. Maycock, T. Waterfield, O. Yelekçi, R. Yu, and B. Z. (eds.), "Climate change 2021: The physical science basis. contribution of working group i to the sixth assessment report of the intergovernmental panel on climate change.," *Cambridge University Press*, 2021.

[6] E. Commission, "Communication from the commission to the european parliament, the council, the european economic and social committee and the committee of the regions," *EU Solar Energy Strategy*, vol. final, 5 2022.

[7] R. Guerrero-Lemus, R. Vega, T. Kim, A. Kimm, and L. Shephard, "Bifacial solar photovoltaics – a technology review," *Renewable and Sustainable Energy Reviews*, vol. 60, pp. 1533–1549, 2016.

[8] H. N. Riise, M. Øgaard, J. Zhu, C. C. You, F. Andersson, T. Bønsnæs, J. Young, and S. E. Foss, "Performance analysis of a bapv bifacial system in norway," in *2021 IEEE 48th Photovoltaic Specialists Conference (PVSC)*, pp. 1304–1308, 2021.

[9] M. Ito and E. Gerritsen, "Geographical mapping of the performance of vertically installed bifacial modules," 06 2016.

[10] X. Sun, M. R. Khan, C. Deline, and M. A. Alam, "Optimization and performance of bifacial solar modules: A global perspective," *Applied energy*, vol. 212, pp. 1601–1610, 2018.

[11] S. R. Wenham and M. A. Green, "Silicon solar cells," *Progress in Photovoltaics: Research and Applications*, vol. 4, 1996.

[12] U. Eicker, *Solar technologies for buildings.* John Wiley & Sons, 2003.

[13] J. Nelson, *The Physics of Solar Cells*. 2003.

[14] F. ISE, "Photovoltaics report," 2022. updated February 2022.

[15] S. S. Kshatri, J. Dhillon, S. Mishra, R. Tariq, N. K. Sharma, M. Bajaj, A. U. Rehman, M. Shafiq, and J.-G. Choi, "Reliability analysis of bifacial pv panel-based inverters considering the effect of geographical location," *Energies*, vol. 15, no. 1, 2022.

[16] G. Raina and S. Sinha, "A simulation study to evaluate and compare monofacial vs bifacial perc pv cells and the effect of albedo on bifacial performance," *Materials Today: Proceedings*, vol. 46, pp. 5242–5247, 2021.

[17] W. A. Badawy, "A review on solar cells from si-single crystals to porous materials and quantum dots," *Journal of Advanced Research*, vol. 6, no. 2, pp. 123–132, 2015.

[18] J. Stein, C. Reise, J. Castro, G. Friesen, G. Mauger, E. Urrejola, S. Ranta, M. Alam, M. Anoma, S. Pelaez, D. Berrian, E. Bertrand, M. Chiodetti, D. Chudinzow, H. Colin, I. Devoto, R. French, E. Fuentealba, F. Haffner, A. Halm, J. Haysom, K. Hinzer, I. Horvath, H. Huerta, M. Khan, M. Klenk, R. Kopecek, J. Libal, M. Lindh, B. Marion, M. Mikofski, R. Molinero, M. Monarch, A. Neubert, M. Patel, A. Petersson, G. Poulin, S. Ramesh, O. Rhazi, N. Riedel-Lyngskær, D. Riley, A. Russell, A. Schneider, C. Stark, T. Timofte, D. Tune, J. Tymchak, C. Valdivia, F. Valencia, and M. Wang, *Bifacial Photovoltaic Modules and Systems: Experience and Results from International Research and Pilot Applications: Report IEA-PVPS T13-14:2021*. International Energy Agency, 2021.

[19] C. Reise and A. Schmid, "Realistic yield expectations for bifacial pv systems – an assessment of announced, predicted and observed benefits," *31st European Photovoltaic Solar Energy Conference and Exhibition*, 2015.

[20] L. Gullbrekken, T. Kvande, and B. Time, "Roof-integrated pv in nordic climate-building physical challenges," *Energy Procedia*, vol. 78, pp. 1962–1967, 2015.

[21] G. Lobaccaro, S. Carlucci, S. Croce, R. Paparella, and L. Finocchiaro, "Boosting solar accessibility and potential of urban districts in the nordic climate: A case study in trondheim," *Solar Energy*, vol. 149, pp. 347–369, 2017.

[22] S. Guo, T. M. Walsh, and M. Peters, "Vertically mounted bifacial photovoltaic modules: A global analysis," *Energy*, vol. 61, pp. 447–454, 2013.

[23] C.B.Honsberg and S.G.Bowden, "Photovoltaics education website." `https://www.pveducation.org`, 2019. Last acessed 08.11.2021

[24] O. A. Katsikogiannis, H. Ziar, and O. Isabella, "Integration of bifacial photovoltaics in agrivoltaic systems: A synergistic design approach," *Applied Energy*, vol. 309, p. 118475, 2022.

[25] Y. Zhang, Y. Yu, F. Meng, and Z. Liu, "Experimental investigation of the shading and mismatch effects on the performance of bifacial photovoltaic modules," *IEEE Journal of Photovoltaics*, vol. 10, no. 1, pp. 296–305, 2020.

[26] C. Deline, S. MacAlpine, B. Marion, F. Toor, A. Asgharzadeh, and J. S. Stein, "Evaluation and field assessment of bifacial photovoltaic module power rating methodologies," in *2016 IEEE 43rd Photovoltaic Specialists Conference (PVSC)*, pp. 3698–3703, 2016.

[27] E. A. Handoyo, D. Ichsani, and Prabowo, "The optimal tilt angle of a solar collector," *Energy Procedia*, vol. 32, pp. 166–175, 2013.

[28] C. D. Rodríguez-Gallegos, M. Bieri, O. Gandhi, J. P. Singh, T. Reindl, and S. Panda, "Monofacial vs bifacial si-based pv modules: Which one is more cost-effective?," *Solar Energy*, vol. 176, pp. 412–438, 2018.

[29] R. Mubarak, E. Weide Luiz, and G. Seckmeyer, "Why pv modules should preferably no longer be oriented to the south in the near future," *Energies*, vol. 12, no. 23, 2019.

[30] A. Goetzberger and V. U. Hoffmann, *Photovoltaic Solar Energy Generation*. Berlin Heidelberg: Springer, 2005.

[31] C. Honsberg and S. Bowden, "Solar cell efficiency." `https://www.pveducation.org/pvcdrom/solar-cell-operation/solar-cell-efficiency`. Last accessed 04.10.2021

[32] P. Singh and N. Ravindra, "Temperature dependence of solar cell performance—an analysis," *Solar Energy Materials & Solar Cells*, 2012.

[33] M. Alonso, J. Balenzategui, and F. Chenlo, "On the noct determination of pv solar modules," in *Sixteenth European Photovoltaic Solar Energy Conference*, pp. 2386–2389, Routledge, 2020.

[34] ABB, "Photovoltaic plants," *Technical application paper*, vol. 10, 2014.

[35] K. Bakirci, "General models for optimum tilt angles of solar panels: Turkey case study," *Renewable and Sustainable Energy Reviews*, vol. 16, no. 8, pp. 6149–6159, 2012.

[36] O. Kehinde, F. Ehiagwina, L. Afolabi, and A. Olaoye, "Photovoltaic cell output voltage variations with time and inclination angle," *IOSR Journal of Electrical and Electronics Engineering*, vol. 11, pp. 40–47, 08 2016.

[37] F. Vignola, "Ghi correlations with dhi and dni and the effects of cloudiness on one-minute data," 2012.

[38] A. Padovan, D. Del Col, V. Sabatelli, and D. Marano, "Dni estimation procedures for the assessment of solar radiation availability in concentrating systems," *Energy Procedia*, vol. 57, pp. 1140–1149, 2014.

[39] Suncurves, "Suncurves in trondheim." `https://suncurves.com/no/v/794/`. Last accessed 05.10.2021

[40] T. C. R. Russell, R. Saive, A. Augusto, S. G. Bowden, and H. A. Atwater, "The influence of spectral albedo on bifacial solar cells: A theoretical and experimental study," *IEEE Journal of Photovoltaics*, vol. 7, no. 6, pp. 1611–1618, 2017.

[41] M. Chiodetti, A. Lindsay, P. Dupeyrat, D. Binesti, E. Lutun, K. Radouane, and S. Mousel, "Pv bifacial yield simulation with a variable albedo model," *the sun*, vol. 1, p. 4, 2016.

[42] M. Chiodetti, A. Lindsay, P. Dupeyrat, D. Binesti, E. Lutun, R. Khalid, and S. Mousel[2], "Pv bifacial yield simulation with a variable albedo model," 06 2016.

[43] C. Reise and A. Schmid, "Realistic yield expectations for bifacial pv systems—an assessment of announced predicted and observed benefits," in *Proc. 31st Eur. Photovolt. Sol. Energy Conf. Exhib*, pp. 1775–1779, 2015.

[44] B. Y. Liu and R. C. Jordan, "The interrelationship and characteristic distribution of direct, diffuse and total solar radiation," *Solar Energy*, vol. 4, no. 3, pp. 1–19, 1960.

[45] B. LeBaron and I. Dirmhirn, "Strengths and limitations of the liu and jordan model to determine diffuse from global irradiance," *Solar Energy*, vol. 31, no. 2, pp. 167–172, 1983.

[46] J. Orgill and K. Hollands, "Correlation equation for hourly diffuse radiation on a horizontal surface," *Solar Energy*, vol. 19, no. 4, pp. 357–359, 1977.

[47] D. Erbs, S. Klein, and J. Duffie, "Estimation of the diffuse radiation fraction for hourly, daily and monthly-average global radiation," *Solar Energy*, vol. 28, no. 4, pp. 293–302, 1982.

[48] D. Reindl, W. Beckman, and J. Duffie, "Diffuse fraction correlations," *Solar Energy*, vol. 45, no. 1, pp. 1–7, 1990.

[49] P. Ineichen, R. Perez, R. Seal, E. Maxwell, and A. Zalenka, "Dynamic global-to-direct irradiance conversion models," *ASHRAE transactions*, vol. 98, no. 1, pp. 354–369, 1992.

[50] A. Skartveit, J. A. Olseth, and M. E. Tuft, "An hourly diffuse fraction model with correction for variability and surface albedo," *Solar Energy*, vol. 63, no. 3, pp. 173–183, 1998.

[51] B. Ridley, J. Boland, and P. Lauret, "Modelling of diffuse solar fraction with multiple predictors," *Renewable Energy*, vol. 35, no. 2, pp. 478–483, 2010.

[52] M. Hofmann and G. Seckmeyer, "A new model for estimating the diffuse fraction of solar irradiance for photovoltaic system simulations," *Energies*, vol. 10, no. 2, 2017.

[53] L. Laiti, L. Giovannini, D. Zardi, G. Belluardo, and D. Moser, "Estimating hourly beam

and diffuse solar radiation in an alpine valley: A critical assessment of decomposition models," *Atmosphere*, vol. 9, no. 4, 2018.

[54] C. A. Gueymard and J. A. Ruiz-Arias, "Extensive worldwide validation and climate sensitivity analysis of direct irradiance predictions from 1-min global irradiance," *Solar Energy*, vol. 128, pp. 1–30, 2016. Special issue: Progress in Solar Energy.

[55] D. Yang, "Estimating 1-min beam and diffuse irradiance from the global irradiance: A review and an extensive worldwide comparison of latest separation models at 126 stations," *Renewable and Sustainable Energy Reviews*, vol. 159, p. 112195, 2022.

[56] B. Liu and R. Jordan, "Daily insolation on surfaces tilted towards equator," *ASHRAE J.; (United States)*, vol. 10, 10 1961.

[57] T. Klucher, "Evaluation of models to predict insolation on tilted surfaces," *Solar Energy*, vol. 23, no. 2, pp. 111–114, 1979.

[58] J. E. Hay, "Calculation of monthly mean solar radiation for horizontal and inclined surfaces," *Solar Energy*, vol. 23, no. 4, pp. 301–307, 1979.

[59] R. Perez, R. Seals, P. Ineichen, R. Stewart, and D. Menicucci, "A new simplified version of the perez diffuse irradiance model for tilted surfaces," *Solar Energy*, vol. 39, no. 3, pp. 221–231, 1987.

[60] D. Reindl, W. Beckman, and J. Duffie, "Evaluation of hourly tilted surface radiation models," *Solar Energy*, vol. 45, no. 1, pp. 9–17, 1990.

[61] M. Lave, W. Hayes, A. Pohl, and C. W. Hansen, "Evaluation of global horizontal irradiance to plane-of-array irradiance models at locations across the united states," *IEEE journal of Photovoltaics*, vol. 5, no. 2, pp. 597–606, 2015.

[62] D. Yang, "Solar radiation on inclined surfaces: Corrections and benchmarks," *Solar Energy*, vol. 136, pp. 288–302, 2016.

[63] V. Software, "Pv*sol premium."

[64] J. Remund, S. Müller, M. Schmutz, and P. Graf, "Meteonorm."

[65] NREL, "Users manual for tmy3 data sets."

[66] M. S. Lave, W. Hayes, C. Hansen, and A. P. Pohl, "Evaluation of irradiance decomposition and transposition models at locations across the united states.," 6 2014.

[67] T. Kato, "Prediction of photovoltaic power generation output and network operation," in *Integration of Distributed Energy Resources in Power Systems*, pp. 77–108, Elsevier, 2016.

[68] R. Einhaus, F. Madon, J. Degoulange, K. Wambach, J. Denafas, F. R. Lorenzo, S. C. Abalde, T. D. García, and A. Bollar, "Recycling and reuse potential of nice pv-modules," 2020.

[69] C. Benjaminsen, "Ny og hoythengende lab skal gi oss supereffektive solceller." `https://gemini.no/2021/09/ny-og-hoythengende-lab-skal-gi-oss-supereffektive-solceller/`, 2021. Last accessed 17.01.2022

[70] G. Van Rossum and F. L. Drake, *Python 3 Reference Manual.* Scotts Valley, CA: CreateSpace, 2009.

[71] J. D. Hunter, "Matplotlib: A 2d graphics environment," *Computing in Science Engineering*, vol. 9, no. 3, pp. 90–95, 2007.

[72] W. McKinney *et al.*, "Data structures for statistical computing in python," in *Proceedings of the 9th Python in Science Conference*, vol. 445, pp. 51–56, Austin, TX, 2010.

A Datasheets and IV parameters

The table below shows the parameters from the panels on Sentralbygg 1. Following are the datasheets for the pyranometers and pyrheliometer used to measure GHI DHI and DNI. The solar cells on Sentralbygg 1 are not commercial yet and therefore do not have datasheets, but the data from a flash test and the area of the cells are attached below.

Module	Isc_(A)	Voc_(V)	Imp_(A)	Vmp_(V)	Pmp_(W)	FF_(percent)
801	9,25	40,4	8,8	33,4	294,5	78,9
822	9,24	40,4	8,8	33,5	294,8	79,0
823	9,28	40,4	8,8	33,5	296,0	78,9
824	9,25	40,4	8,8	33,5	295,1	78,9
825	9,25	40,4	8,8	33,5	295,0	78,8
834	9,29	40,4	8,8	33,5	295,3	78,7
857	9,28	40,4	8,8	33,5	295,5	78,9
859	9,26	40,3	8,8	33,5	294,8	78,9
860	9,29	40,4	8,8	33,5	295,3	78,7

Figure A.1: Data from a flash test that was conducted on the panels at Sentralbygg 1.

Technical Specifications

	CMP10 | CMP11	SMP10 | SMP11
Classification to ISO 9060:2018	Spectrally Flat Class A	Spectrally Flat Class A
Sensitivity	7 to 14 µV/W/m²	-
Impedance	10 to 100 Ω	-
Expected output range (0 to 1500 W/m²)	0 to 20 mV	-
Maximum operational irradiance	4000 W/m²	-
Analog output • V-version	-	0 to 1 V
Analog output range*	-	-200 to 2000 W/m²
Analog output • A-version	-	4 to 20 mA
Analog output range*	-	0 to 1600 W/m²
Serial output	-	RS-485 Modbus®
Serial output range	-	-400 to 4000 W/m²
Response time (63 %)	< 1.7 s	< 0.7 s
Response time (95 %)	< 5 s	< 2 s
Spectral range (20 % points)	270 to 3000 nm	270 to 3000 nm
Spectral range (50 % points)	285 to 2800 nm	285 to 2800 nm
Zero offsets (unventilated) (a) thermal radiation (at 200 W/m²) (b) temperature change (5 K/h)	< 7 W/m² < 2 W/m²	< 7 W/m² < 2 W/m²
Non-stability (change/year)	< 0.5 %	< 0.5 %
Non-linearity (100 to 1000 W/m²)	< 0.2 %	< 0.2 %
Directional response (up to 80 ° with 1000 W/m² beam)	< 10 W/m²	< 10 W/m²
Spectral selectivity (350 to 1500 nm)	< 3 %	< 3 %
Tilt response (0 ° to 90 ° at 1000 W/m²)	< 0.2 %	< 0.2 %
Temperature response	< 1 % (-10 °C to +40 °C)	< 1 % (-20°C to +50 °C) < 2 % (-40 °C to +70 °C)
Field of view	180 °	180 °
Accuracy of bubble level	< 0.1 °	< 0.1 °
Power consumption (at 12 VDC)	-	V-version: 55 mW A-version: 100 mW
Supply voltage	-	5 to 30 VDC
Software, Windows™	-	SmartExplorer Software, for configuration, test and data logging
Detector type	Thermopile	Thermopile
Operating and storage temperature range	-40 °C to +80 °C	-40 °C to +80 °C
Humidity range	0 to 100 %	0 to 100 %
MTBF (Mean Time Between Failures)	> 10 years	> 10 years **
Ingress Protection (IP) rating	67	67
Recommended applications	Meteorological networks, PV panel and thermal collector testing, materials testing	High performance for PV panel and thermal collector testing, solar energy research, solar prospecting, materials testing, advanced meteorology and climate networks

Note: The performance specifications quoted are worst-case and/or maximum values.

* adjustable with SmartExplorer Software | ** extrapolated after introduction in January 2012

Dimensions

CMP10 | SMP10
Ø 50 mm
68 mm
Ø 150 mm

CMP11 | SMP11
Ø 50 mm
68 mm
Ø 150 mm
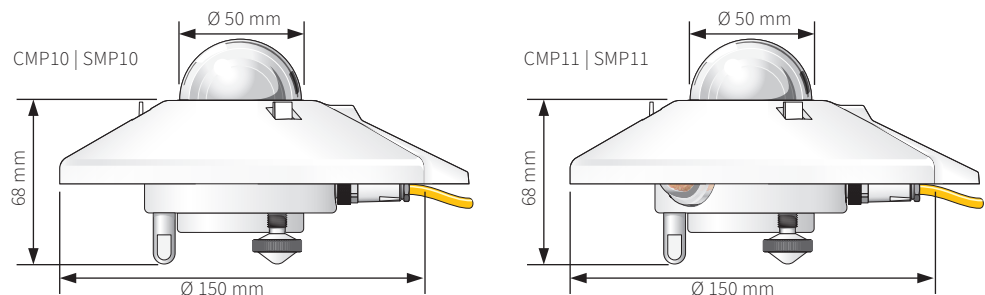
Technical Specifications

	CHP1	SHP1
Classification to ISO 9060:2018	Spectrally Flat Class A	Spectrally Flat Class A
Sensitivity	7 to 14 µV/W/m²	-
Expected output range (0 to 1400 W/m²)	10 to 20 mV	-
Maximum operational irradiance	4000 W/m²	-
Analog output • V-version	-	0 to 1 V
Analog output range*	-	-200 to 2000W/m²
Analog output • A-version	-	4 to 20 mA
Analog output range*	-	0 to 1600 W/m²
Serial output	-	RS-485 Modbus® RTU
Serial output range	-	-400 to 4000 W/m²
Response time (63 %)	< 1.7 s	< 0.7 s
Response time (95 %)	< 5 s	< 2 s
Spectral range (50 % points)	200 to 4000 nm	200 to 4000 nm
Zero offsets (unventilated) (b) temperature change (5 K/h)	< 1 W/m²	< 1 W/m²
Non-stability (change/year)	< 0.5 %	< 0.5 %
Non-linearity (0 to 1000 W/m²)	< 0.2 %	< 0.2 %
Spectral selectivity (350 to 1500 nm)	< 1 %	< 1 %
Required sun tracker accuracy	< 0.5 ° from ideal	< 0.5 ° from ideal
Weight (excluding cable)	0.9 kg	0.9 kg
Slope angle	1 ° ±0.2 °	1 ° ±0.2 °
Temperature response	< 0.5 % (-20 °C to +50 °C)	< 0.5 % (-30 °C to +60 °C) < 1 % (-40 °C to +70 °C)
Field of view	5 ° ±0.2 °	5 ° ±0.2 °
Power consumption (at 12 VDC)	-	V-version: 55 mW A-version: 100 mW
Supply voltage	-	5 to 30 VDC
Software, Windows™	-	SmartExplorer Software, for configuration, test and data logging
Operating and storage temperature range	-40 °C to +80 °C	-40 °C to +80 °C
Humidity range	0 to 100 %	0 to 100 %
MTBF (Mean Time Between Failures) **	> 10 years	> 10 years
Ingress Protection (IP) rating	67	67
Recommended applications	High performance direct radiation monitoring for meteorological stations or concentrated solar energy applications	High performance direct radiation monitoring for meteorological stations or concentrated solar energy applications

Note: The performance specifications quoted are worst-case and/or maximum values.

* adjustable with SmartExplorer Software

Dimensions

74 mm

322 mm

⌀38 mm

76 mm
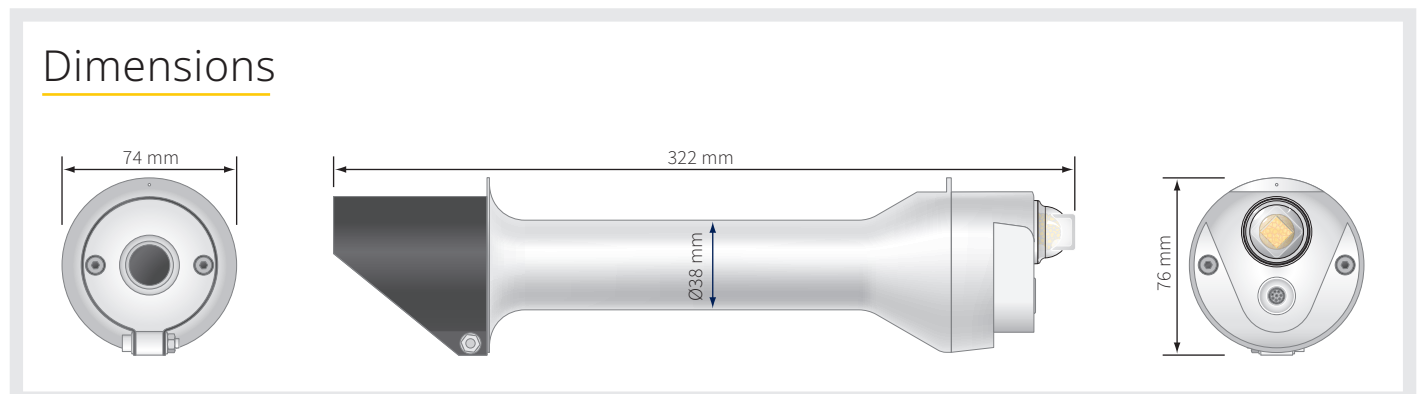
B Relative Root Mean Square Deviation

Table B.1: S 44 3D October

Transposition / DHI model	Liu & Jordan	Hay & Davies	Klucher	Perez	Reindl
Orgill & Hollands	31.66	29.94	28.4	28.38	29.87
Erbs, Klein & Duffe	29.91	31.14	29.85	30.88	31.21
Reindl	38.98	32.81	32.36	29.67	32.48
Perez & Inceichen	32.97	30.97	29.84	30.35	30.9
Skartveit	34.32	32.8	31.32	31.2	32.32
Boland, Ridley & Laurent	36.53	32.48	31.65	29.99	32.25
Hoffman	35.59	31.64	30.77	29.52	31.44

Table B.2: V E/W 3D October

Transposition / DHI model	Liu & Jordan	Hay & Davies	Klucher	Perez	Reindl
Orgill & Hollands	71.4	68.63	64.46	63.92	65.31
Erbs, Klein & Duffe	65.03	63.64	60.26	56.92	61.6
Reindl	73.95	71.25	65.79	66.43	66.57
Perez & Inceichen	72.3	69.29	64.74	64.99	65.57
Skartveit	71.65	67.77	64.99	64.66	65.63
Boland, Ridley & Laurent	75.81	72.49	67.56	67.29	68.1
Hoffman	74.86	71.51	66.42	66.47	67.07

Table B.3: V S/N 3D October

Transposition / DHI model	Liu & Jordan	Hay & Davies	Klucher	Perez	Reindl
Orgill & Hollands	32.7	32.96	31.39	32.29	33.11
Erbs, Klein & Duffe	34.81	36.72	36.48	37.3	37.21
Reindl	40.38	35.63	33.58	33.22	34.6
Perez & Inceichen	35.02	34.62	33.47	34.75	34.74
Skartveit	36.49	36.86	34.71	35.61	35.92
Boland, Ridley & Laurent	37.82	35.2	33.35	33.58	34.54
Hoffman	37.07	34.69	33.07	33.44	34.3

Table B.4: S 44 3D November

Transposition DHI model	Liu & Jordan	Hay & Davies	Klucher	Perez	Reindl
Orgill & Hollands	53.31	42.4	48.06	46.02	42.21
Erbs, Klein & Duffe	72.49	64.68	68.79	47.86	64.47
Reindl	57.07	52.24	54.37	51.78	52.07
Perez & Inceichen	47.75	46.95	45.55	44.72	46.95
Skartveit	53.65	46.54	50.77	41.44	47.74
Boland, Ridley & Laurent	56.4	52.86	53.67	51.16	52.73
Hoffman	55.94	52.34	53.08	50.88	52.22

Table B.5: V E/W 3D November

Transposition DHI model	Liu & Jordan	Hay & Davies	Klucher	Perez	Reindl
Orgill & Hollands	61.15	54.41	58.2	45.48	53.95
Erbs, Klein & Duffe	89.32	88.89	85.75	42.13	86.69
Reindl	52.14	53.15	52.32	46.72	53.12
Perez & Inceichen	50.03	51.31	50.52	44.03	51.53
Skartveit	76.79	74.62	74.25	43.84	73.87
Boland, Ridley & Laurent	50.69	52.59	51.16	45.55	52.61
Hoffman	50.54	52.54	51.04	45.45	52.56

Table B.6: V S/N 3D November

Transposition DHI model	Liu & Jordan	Hay & Davies	Klucher	Perez	Reindl
Orgill & Hollands	60.62	44.29	50.7	38.9	43.26
Erbs, Klein & Duffe	82.84	71.79	75.42	41.29	70.83
Reindl	52.64	46.55	47.87	40.51	45.83
Perez & Inceichen	47.01	43.7	43.12	36.23	43.27
Skartveit	66.04	54.62	60.32	35.34	56.77
Boland, Ridley & Laurent	53.73	47.84	49.05	41.36	47.08
Hoffman	53.39	47.29	48.47	41.02	46.53

Table B.7: S 44 3D October and November

Transposition / DHI model	Liu & Jordan	Hay & Davies	Klucher	Perez	Reindl
Orgill & Hollands	41.64	35.94	37.32	37.41	35.81
Erbs, Klein & Duffe	48.37	45.78	46.27	39.06	45.71
Reindl	50.18	44.89	45.75	43.61	44.65
Perez & Inceichen	40.86	39.95	38.03	38.2	39.92
Skartveit	43.17	39.28	40.05	36.44	39.47
Boland, Ridley & Laurent	48.07	44.66	44.22	42.65	44.49
Hoffman	47.32	43.95	43.38	42.18	43.79

Table B.8: V E/W 3D October and November

Transposition / DHI model	Liu & Jordan	Hay & Davies	Klucher	Perez	Reindl
Orgill & Hollands	68.72	64.48	62.83	57.26	62
Erbs, Klein & Duffe	70.01	68.64	65.32	51.64	66.52
Reindl	64.92	63.52	60.48	57.14	61.03
Perez & Inceichen	64.91	62.54	60.16	56.62	60.43
Skartveit	72.91	69.57	67.2	56.76	67.7
Boland, Ridley & Laurent	66.15	64.2	61.49	57.46	61.85
Hoffman	65.61	63.65	60.81	57.03	61.26

Table B.9: V S/N 3D October and November

Transposition / DHI model	Liu & Jordan	Hay & Davies	Klucher	Perez	Reindl
Orgill & Hollands	47.51	39.05	41.14	35.84	38.49
Erbs, Klein & Duffe	57.99	53.68	54.38	39.28	53.25
Reindl	48.53	42.79	42.67	37.96	41.84
Perez & Inceichen	42.15	40.13	38.89	35.59	39.82
Skartveit	52.2	46.38	47.75	35.46	46.84
Boland, Ridley & Laurent	47.96	43.2	42.92	38.44	42.36
Hoffman	47.39	42.61	42.33	38.12	41.86

Table B.10: S 44 2D October

Transposition / DHI model	Liu & Jordan	Hay & Davies	Klucher	Perez	Reindl
Orgill & Hollands	31.28	29.75	28.14	28.23	29.69
Erbs, Klein & Duffe	29.77	31.01	29.76	30.74	31.09
Reindl	38.7	32.81	32.26	29.8	32.5
Perez & Inceichen	32.58	30.75	29.56	30.1	30.69
Skartveit	33.96	32.67	31.05	31.11	32.14
Boland, Ridley & Laurent	35.93	32.07	31.13	29.83	31.85
Hoffman	35.04	31.3	30.34	29.31	31.12

Table B.11: V E/W 2D October

Transposition / DHI model	Liu & Jordan	Hay & Davies	Klucher	Perez	Reindl
Orgill & Hollands	69.32	66.83	62.8	62.48	63.72
Erbs, Klein & Duffe	64.78	63.5	60.07	56.67	61.48
Reindl	71.46	69.17	64.12	64.81	64.96
Perez & Inceichen	70.28	67.47	63.08	63.45	63.96
Skartveit	69.6	66.16	63.35	63.61	64.08
Boland, Ridley & Laurent	73.76	70.54	65.79	65.53	66.36
Hoffman	72.76	69.55	64.67	64.75	65.34

Table B.12: V S/N 2D October

Transposition / DHI model	Liu & Jordan	Hay & Davies	Klucher	Perez	Reindl
Orgill & Hollands	32.65	32.98	31.4	32.32	33.14
Erbs, Klein & Duffe	34.75	36.62	36.44	37.2	37.12
Reindl	40.82	36.14	34.08	33.77	35.09
Perez & Inceichen	34.88	34.55	33.39	34.64	34.69
Skartveit	36.4	36.89	34.68	35.68	35.94
Boland, Ridley & Laurent	37.56	35.02	33.14	33.63	34.38
Hoffman	36.85	34.56	32.91	33.4	34.18

Table B.13: Tracking 2D October

Transposition / DHI model	Liu & Jordan	Hay & Davies	Klucher	Perez	Reindl
Orgill & Hollands	40.93	38.8	37.2	37.31	38.61
Erbs, Klein & Duffe	38.1	38.75	37.63	37.86	38.86
Reindl	51.26	42.98	43.21	39.49	42.15
Perez & Inceichen	42.7	39.75	38.76	39.17	39.54
Skartveit	44.06	41.92	40.53	40.55	41.27
Boland, Ridley & Laurent	47.56	41.56	41.28	38.92	40.94
Hoffman	46.36	40.62	40.22	38.38	40.1

Table B.14: 44 S 2D November

Transposition / DHI model	Liu & Jordan	Hay & Davies	Klucher	Perez	Reindl
Orgill & Hollands	50.47	40.59	45.41	44.33	40.44
Erbs, Klein & Duffe	72.11	64.4	68.38	47.7	64.18
Reindl	56.15	51.98	53.69	51.64	51.84
Perez & Inceichen	46.03	46.39	44.06	43.9	46.42
Skartveit	53.74	46.99	50.89	42.24	48.08
Boland, Ridley & Laurent	54.9	52.39	52.42	50.58	52.29
Hoffman	54.42	51.92	51.83	50.31	51.82

Table B.15: V E/W 2D November

Transposition / DHI model	Liu & Jordan	Hay & Davies	Klucher	Perez	Reindl
Orgill & Hollands	54.64	51.05	53.1	44.85	51.16
Erbs, Klein & Duffe	87.78	87.46	84.37	42.56	85.33
Reindl	55.39	56.49	55.57	51.16	56.46
Perez & Inceichen	48.79	53.01	49.94	45.17	53.34
Skartveit	76.33	75.02	74.13	46.22	74.1
Boland, Ridley & Laurent	52.31	55.64	52.97	48.96	55.69
Hoffman	52.09	55.61	52.8	48.85	55.66

Table B.16: V S/N 2D November

Transposition DHI model	Liu & Jordan	Hay & Davies	Klucher	Perez	Reindl
Orgill & Hollands	58.45	43.1	48.84	37.65	42.18
Erbs, Klein & Duffe	82.88	71.83	75.35	40.88	70.85
Reindl	52.58	47.23	48.21	41.54	46.57
Perez & Inceichen	46.0	44.05	42.5	36.05	43.7
Skartveit	66.39	55.28	60.7	36.32	57.34
Boland, Ridley & Laurent	53.13	48.19	48.91	41.9	47.49
Hoffman	52.78	47.71	48.36	41.63	47.01

Table B.17: Tracking 2D November

Transposition DHI model	Liu & Jordan	Hay & Davies	Klucher	Perez	Reindl
Orgill & Hollands	62.24	45.89	55.54	37.80	45.38
Erbs, Klein & Duffe	91.03	78.24	85.46	40.11	77.59
Reindl	53.63	48.33	50.83	40.65	47.99
Perez & Inceichen	48.05	46.29	45.85	36.25	46.13
Skartveit	72.59	60.37	68.61	36.58	63.04
Boland, Ridley & Laurent	54.46	49.17	51.67	41.04	48.8
Hoffman	54.19	48.71	51.28	40.86	48.35

Table B.18: 44 S 2D Oct and Nov

Transposition DHI model	Liu & Jordan	Hay & Davies	Klucher	Perez	Reindl
Orgill & Hollands	40.16	35.02	35.99	36.56	34.92
Erbs, Klein & Duffe	48.1	45.56	46	38.91	45.49
Reindl	49.77	45.01	45.61	43.8	44.78
Perez & Inceichen	39.88	39.75	37.24	37.75	39.74
Skartveit	43.05	39.46	40	36.85	39.57
Boland, Ridley & Laurent	47.24	44.56	43.6	42.48	44.41
Hoffman	46.51	43.91	42.8	42.02	43.77

Table B.19: V E/W 2D Oct and Nov

Transposition / DHI model	Liu & Jordan	Hay & Davies	Klucher	Perez	Reindl
Orgill & Hollands	65.26	61.77	60.12	55.65	59.71
Erbs, Klein & Duffe	69.5	68.25	64.9	51.53	66.17
Reindl	63.81	62.96	60.23	57.7	60.93
Perez & Inceichen	62.21	61.16	58.28	55.49	59.44
Skartveit	71.31	68.59	66.02	56.81	66.7
Boland, Ridley & Laurent	64.12	63.25	60.24	57.14	61.28
Hoffman	63.58	62.76	59.61	56.75	60.78

Table B.20: V S/N 2D Oct and Nov

Transposition / DHI model	Liu & Jordan	Hay & Davies	Klucher	Perez	Reindl
Orgill & Hollands	46.43	38.48	40.25	35.22	37.99
Erbs, Klein & Duffe	57.97	53.63	54.3	39.03	53.2
Reindl	48.78	43.54	43.24	38.9	42.64
Perez & Inceichen	41.61	40.46	38.61	35.46	40.21
Skartveit	52.41	46.8	47.98	36.03	47.2
Boland, Ridley & Laurent	47.77	43.58	43.04	38.92	42.78
Hoffman	47.22	43.04	42.48	38.63	42.33

Table B.21: Tracking 2D Oct and Nov

Transposition / DHI model	Liu & Jordan	Hay & Davies	Klucher	Perez	Reindl
Orgill & Hollands	51.27	42.34	45.87	37.56	41.98
Erbs, Klein & Duffe	61.57	56.26	58.23	38.91	55.98
Reindl	52.76	46.31	47.91	40.21	45.77
Perez & Inceichen	45.75	43.58	42.68	37.58	43.38
Skartveit	57.87	50.96	53.83	38.58	51.81
Boland, Ridley & Laurent	51.82	46.16	47.53	40.19	45.68
Hoffman	51.18	45.49	46.81	39.85	45.03

C Relative Mean Bias Deviation

Table C.1: S 44 3D October rMBD

DHI model / Transposition	Liu & Jordan	Hay & Davies	Klucher	Perez	Reindl
Orgill & Hollands	7.51	-0.61	1.36	-6.5	-1.22
Erbs, Klein & Duffe	-0.87	-8.56	-6.97	-15.07	-9.09
Reindl	13.19	5.6	6.84	-1.33	4.86
Perez & Inceichen	5.6	-2.76	-1.08	-8.17	-3.45
Skartveit	4.32	-7.49	-1.96	-9.16	-4.11
Boland, Ridley & Laurent	11.83	4.5	6.06	-2.11	3.84
Hoffman	9.61	1.65	2.95	-5.12	0.9

Table C.2: V E/W 3D October rMBD

DHI model / Transposition	Liu & Jordan	Hay & Davies	Klucher	Perez	Reindl
Orgill & Hollands	1.26	-1.32	-7.15	-6.5	-6.71
Erbs, Klein & Duffe	1.78	0.02	-5.97	-15.07	-4.62
Reindl	3.7	1.77	-4.63	-1.33	-4.87
Perez & Inceichen	1.91	-0.56	-7.04	-8.17	-6.74
Skartveit	0.17	-3.97	-8.4	-9.16	-8.4
Boland, Ridley & Laurent	4.67	2.67	-2.92	-2.11	-3.24
Hoffman	3.7	1.5	-5.12	-5.12	-5.27

Table C.3: V S/N 3D October rMBD

DHI model / Transposition	Liu & Jordan	Hay & Davies	Klucher	Perez	Reindl
Orgill & Hollands	-2.38	-12.23	-13.97	-20	-16.07
Erbs, Klein & Duffe	-12.71	-21.99	-24.28	-30.97	-25.29
Reindl	4.87	-4.31	-6.86	-12.92	-9.04
Perez & Inceichen	-4.74	-14.86	-17.28	-22.05	-19.26
Skartveit	-6.49	-20.84	-18.25	-23.41	-20.21
Boland, Ridley & Laurent	3.27	-5.59	-7.45	-13.99	-9.79
Hoffman	0.4	-9.23	-11.96	-17.83	-14.04

Table C.4: S 44 3D November

Transposition / DHI model	Liu & Jordan	Hay & Davies	Klucher	Perez	Reindl
Orgill & Hollands	21.94	8.58	17.82	-3.11	8.01
Erbs, Klein & Duffe	26.07	18.47	23.06	-8.24	18.13
Reindl	10.5	0.75	6.95	-11.99	0.27
Perez & Inceichen	11.21	-1.22	7.44	-10.5	-1.75
Skartveit	21.75	7.61	18.51	-9.61	12.74
Boland, Ridley & Laurent	14.13	3.6	10.76	-8.22	3.12
Hoffman	12.89	1.7	9.16	-10.03	1.17

Table C.5: V E/W 3D November

Transposition / DHI model	Liu & Jordan	Hay & Davies	Klucher	Perez	Reindl
Orgill & Hollands	6.87	0.56	0.08	-27.15	-3.78
Erbs, Klein & Duffe	19.78	19.86	15.67	-26.17	17.21
Reindl	-7.08	-10.18	-12.63	-37.56	-14.38
Perez & Inceichen	-1.83	-7.71	-7.96	-32.25	-11.81
Skartveit	11.88	7.67	6.86	-30.73	5.68
Boland, Ridley & Laurent	-4.08	-8.26	-9.41	-34.98	-12.2
Hoffman	-4.22	-8.67	-10.13	-35.32	-13.1

Table C.6: V S/N 3D November

Transposition / DHI model	Liu & Jordan	Hay & Davies	Klucher	Perez	Reindl
Orgill & Hollands	30.88	17.67	24.19	5.45	16
Erbs, Klein & Duffe	35.57	28.16	30.7	0.96	27.12
Reindl	20.65	11.5	15.08	-2.06	9.92
Perez & Inceichen	20.02	8.17	13.92	-2.12	6.64
Skartveit	31.06	17.23	25.86	-0.6	21.24
Boland, Ridley & Laurent	23.6	14.2	18.32	1.1	12.75
Hoffman	22.25	12.19	16.39	-0.81	10.56

Table C.7: S 44 3D Oct + Nov

Transposition / DHI model	Liu & Jordan	Hay & Davies	Klucher	Perez	Reindl
Orgill & Hollands	13.7	3.33	8.43	-5.04	2.74
Erbs, Klein & Duffe	10.69	3.04	5.92	-12.14	2.59
Reindl	12.04	3.52	6.89	-5.9	2.89
Perez & Inceichen	8.01	-2.1	2.58	-9.17	-2.72
Skartveit	11.8	-1.01	6.83	-9.35	3.12
Boland, Ridley & Laurent	12.82	4.12	8.08	-4.73	3.53
Hoffman	11.02	1.67	5.61	-7.23	1.02

Table C.8: V E/W 3D Oct + Nov

Transposition / DHI model	Liu & Jordan	Hay & Davies	Klucher	Perez	Reindl
Orgill & Hollands	3.14	-0.69	-4.73	-13.88	-5.73
Erbs, Klein & Duffe	7.81	6.66	1.28	-14.37	2.69
Reindl	0.09	-2.23	-7.31	-14.89	-8.06
Perez & Inceichen	0.66	-2.95	-7.35	-15	-8.44
Skartveit	4.09	-0.07	-3.29	-15.53	-3.68
Boland, Ridley & Laurent	1.74	-0.99	-5.1	-13.57	-6.24
Hoffman	1.05	-1.91	-6.79	-14.58	-7.89

Table C.9: V S/N 3D Oct+Nov

Transposition / DHI model	Liu & Jordan	Hay & Davies	Klucher	Perez	Reindl
Orgill & Hollands	14.61	3.05	5.53	-7	0.32
Erbs, Klein & Duffe	11.96	3.63	3.82	-14.66	1.49
Reindl	12.93	3.76	4.35	-7.37	0.65
Perez & Inceichen	7.91	-3.09	-1.34	-11.87	-6.03
Skartveit	12.7	-1.39	4.29	-11.76	0.97
Boland, Ridley & Laurent	13.66	4.52	5.72	-6.28	1.73
Hoffman	11.56	1.72	2.52	-9.13	-1.47

Table C.10: S 44 2D October

Transposition DHI model	Liu & Jordan	Hay & Davies	Klucher	Perez	Reindl
Orgill & Hollands	5.39	-2.80	-0.95	-9.07	-3.43
Erbs, Klein & Duffe	-3.04	-10.70	-9.27	-17.64	-11.25
Reindl	10.87	3.25	4.34	-4.13	2.5
Perez & Inceichen	3.50	-4.92	-3.38	-10.63	-5.64
Skartveit	2.18	-9.77	-4.29	-11.73	-6.35
Boland, Ridley & Laurent	9.81	2.43	3.86	-4.62	1.75
Hoffman	7.50	-0.52	0.65	-7.63	-1.3

Table C.11: V E/W 2D October

Transposition DHI model	Liu & Jordan	Hay & Davies	Klucher	Perez	Reindl
Orgill & Hollands	-1.96	-4.71	-10.78	-10.74	-10.3
Erbs, Klein & Duffe	-1.20	-2.96	-9.2	-11.75	-7.7
Reindl	-0.04	-2.05	-8.71	-7.53	-8.9
Perez & Inceichen	-1.26	-3.92	-10.64	-9.92	-10.31
Skartveit	-3.19	-7.65	-12.16	-11.73	-12.16
Boland, Ridley & Laurent	1.72	-0.44	-6.25	-6.18	-6.55
Hoffman	0.51	-1.90	-8.71	-7.72	-8.88

Table C.12: V S/N 2D October

Transposition DHI model	Liu & Jordan	Hay & Davies	Klucher	Perez	Reindl
Orgill & Hollands	-4.18	-14.13	-16.11	-22.55	-18.08
Erbs, Klein & Duffe	-14.57	-23.84	-26.36	-33.56	-27.2
Reindl	2.82	-6.40	-9.20	-15.77	-11.25
Perez & Inceichen	-6.51	-16.74	-19.42	-24.5	-21.26
Skartveit	-8.33	-22.88	-20.44	-26	-22.29
Boland, Ridley & Laurent	1.63	-7.32	-9.40	-16.44	-11.64
Hoffman	-1.36	-11.10	-14.07	-20.29	-16.04

Table C.13: Tracking 2D October

Transposition / DHI model	Liu & Jordan	Hay & Davies	Klucher	Perez	Reindl
Orgill & Hollands	4.88	-6.82	-3.41	-15.76	-8.49
Erbs, Klein & Duffe	-4.04	-14.47	-12.01	-24.9	-15.88
Reindl	12.88	2.19	4.55	-8.52	0.16
Perez & Inceichen	2.83	-9.14	-6.11	-17.37	-11.04
Skartveit	0.37	-16.89	-8.07	-19.56	-12.72
Boland, Ridley & Laurent	12.23	1.84	4.60	-8.36	0.02
Hoffman	8.74	-2.60	-0.07	-12.83	-4.67

Table C.14: S 44 2D November

Transposition / DHI model	Liu & Jordan	Hay & Davies	Klucher	Perez	Reindl
Orgill & Hollands	19.40	5.54	15.13	-6.84	4.95
Erbs, Klein & Duffe	25.64	18.11	22.59	-8.89	17.77
Reindl	6.58	-3.34	2.94	-16.36	-3.83
Perez & Inceichen	8.05	-4.92	4.14	-14.37	-5.47
Skartveit	20.25	5.95	16.93	-11.77	11.15
Boland, Ridley & Laurent	10.73	-0.17	7.27	-12.15	-0.66
Hoffman	9.45	-2.13	5.62	-14.01	-2.67

Table C.15: V E/W 2D November

Transposition / DHI model	Liu & Jordan	Hay & Davies	Klucher	Perez	Reindl
Orgill & Hollands	1.52	-5.88	-5.74	-34.7	-10.47
Erbs, Klein & Duffe	18.72	18.87	14.54	-28.26	16.18
Reindl	-15.43	-18.99	-21.24	-46.97	-23.34
Perez & Inceichen	-8.62	-15.67	-15.17	-40.24	-19.96
Skartveit	8.69	4.1	3.43	-35.42	2.13
Boland, Ridley & Laurent	-11.31	-16.34	-16.9	-43.34	-20.41
Hoffman	-11.53	-16.89	-17.72	-43.84	-21.46

Table C.16: V S/N 2D November

Transposition / DHI model	Liu & Jordan	Hay & Davies	Klucher	Perez	Reindl
Orgill & Hollands	28.85	15.10	21.9	1.97	13.35
Erbs, Klein & Duffe	35.52	28.17	30.6	0.37	27.12
Reindl	17.65	8.30	11.9	-5.84	6.68
Perez & Inceichen	17.30	4.87	10.97	-5.8	3.28
Skartveit	29.99	15.96	24.64	-2.68	20.02
Boland, Ridley & Laurent	20.61	11.28	15.17	-2.62	9.79
Hoffman	19.21	9.21	13.19	-4.64	7.53

Table C.17: Tracking 2D November

Transposition / DHI model	Liu & Jordan	Hay & Davies	Klucher	Perez	Reindl
Orgill & Hollands	31.17	16.15	26.56	0.84	15.1
Erbs, Klein & Duffe	39.74	32.07	36.61	0.07	31.46
Reindl	20.00	10.10	16.25	-6.51	9.18
Perez & Inceichen	18.77	5.70	14.6	-7.28	4.79
Skartveit	33.09	18.06	29.59	-3.87	23.13
Boland, Ridley & Laurent	22.81	13.34	19.35	-3.25	12.49
Hoffman	21.27	11.15	17.42	-5.37	10.2

Table C.18: S 44 2D Oct and Nov

Transposition / DHI model	Liu & Jordan	Hay & Davies	Klucher	Perez	Reindl
Orgill & Hollands	11.41	0.78	5.95	-8.11	0.17
Erbs, Klein & Duffe	9.27	1.66	4.41	-13.88	1.21
Reindl	9.03	0.42	3.74	-9.38	-0.22
Perez & Inceichen	5.45	-4.92	-0.15	-12.24	-5.57
Skartveit	9.94	-3.02	4.8	-11.75	1.16
Boland, Ridley & Laurent	10.20	1.31	5.32	-7.86	0.71
Hoffman	8.34	-1.21	2.78	-10.37	-1.89

Table C.19: V E/W 2D Oct and Nov

Transposition / DHI model	Liu & Jordan	Hay & Davies	Klucher	Perez	Reindl
Orgill & Hollands	-0.79	-5.11	-9.09	-18.76	-10.36
Erbs, Klein & Duffe	5.47	4.35	-1.25	-17.28	0.29
Reindl	-5.19	-7.72	-12.9	-20.74	-13.74
Perez & Inceichen	-3.73	-7.85	-12.15	-20.07	-13.54
Skartveit	0.79	-3.71	-6.94	-19.66	-7.38
Boland, Ridley & Laurent	-2.64	-5.76	-9.81	-18.63	-11.19
Hoffman	-3.52	-6.92	-11.73	-19.81	-13.09

Table C.20: V S/N 2D Oct and Nov

Transposition / DHI model	Liu & Jordan	Hay & Davies	Klucher	Perez	Reindl
Orgill & Hollands	12.69	0.81	3.31	-10.02	-2.02
Erbs, Klein & Duffe	11.02	2.74	2.74	-16.23	0.56
Reindl	10.40	1.11	1.58	-10.7	-2.09
Perez & Inceichen	5.65	-5.70	-3.89	-14.95	-8.72
Skartveit	11.25	-3.04	2.6	-14.08	-0.67
Boland, Ridley & Laurent	11.33	2.19	3.15	-9.38	-0.69
Hoffman	9.15	-0.72	-0.14	-12.29	-4.0

Table C.21: Tracking 2D Oct and Nov

Transposition / DHI model	Liu & Jordan	Hay & Davies	Klucher	Perez	Reindl
Orgill & Hollands	17.60	4.30	11.1	-7.72	2.93
Erbs, Klein & Duffe	17.15	8.06	11.52	-12.82	7.03
Reindl	16.33	6.02	10.21	-7.55	4.52
Perez & Inceichen	10.54	-1.96	3.92	-12.49	-3.38
Skartveit	16.21	0.03	10.16	-11.97	4.63
Boland, Ridley & Laurent	17.35	7.41	11.74	-5.89	6.06
Hoffman	14.80	4.06	8.4	-9.22	2.53